Author Manuscript

Author Manuscript

Author Manuscript

Author Manuscript

HHS Public Access

Author manuscript

Concepts Magn Reson Part B Magn Reson Eng. Author manuscript; available in PMC 2019 April 01.

Published in final edited form as:

Concepts Magn Reson Part B Magn Reson Eng. 2018 April ; 48B(2): . doi:10.1002/cmr.b.21384.

Tabletop 700 MHz electron paramagnetic resonance imaging spectrometer

Laura A. Buchanan[1], **George A. Rinard**[2], **Richard W. Quine**[2], **Sandra S. Eaton**[1], and **Gareth R. Eaton**[1]

[1]Department of Chemistry and Biochemistry and Center for EPR Imaging of In Vivo Physiology, University of Denver, Denver, CO 80210

[2]School of Engineering and Computer Science and Center for EPR Imaging of In Vivo Physiology, University of Denver, Denver, CO 80210

Abstract

Low frequency electron paramagnetic resonance imaging is a powerful tool to non-invasively measure the physiological status of tumors. Here, we report on the design and functionality of a rapid scan and pulse table-top imaging spectrometer based around an arbitrary waveform generator and 25mm cross-loop resonator operating at 700 MHz. Two and four-dimensional rapid scan spectral-spatial images are presented. This table-top imager is a prototype for future pre-clinical imagers.

1. Introduction

Electron paramagnetic resonance (EPR) imaging uses magnetic field gradients to spatially encode signals from free radicals. With selection of proper EPR probes, this permits imaging of oxygen concentration, redox, and pH status in vivo and provides crucial information about the environment in tumors.[1–8] Rapid scan (RS) EPR has been shown to yield higher signal to noise than conventional continuous wave (CW) EPR.[9,10] Signal to noise decreases linearly with increasing gradient in rapid scan. In conventional CW, the signal to noise decreases more rapidly, as the square of the gradient. For these reasons, rapid scan EPR imaging is preferred over CW imaging.

Selection of an RF frequency for in vivo imaging involves multiple tradeoffs. If the sample region imaged increases with the inverse of the frequency and the number of voxels and resonator filling factor are kept constant, the EPR signal increases as the frequency is decreased.[11] However, the goal usually is to image a constant small volume element (voxel), and for this case the EPR signal increases with increase in frequency.[12–14] Depth of penetration is greater at lower frequency.[15] For many animal and eventual human studies the Halpern and Krishna laboratories chose 250 and 300 MHz as a reasonable tradeoff of depth of penetration and signal amplitude.[16,17] For a focus on studies of mice, this tradeoff results in selection of a higher frequency. Reviews provide comprehensive citation of low frequency

Corresponding author Professor Gareth R. Eaton, Department of Chemistry and Biochemistry, University of Denver, Denver, CO 80210, geaton@du.edu, Phone: 303-871-2980.

Author Manuscript Author Manuscript Author Manuscript Author Manuscript

EPR spectrometers.[18–20] Several labs have chosen approximately 700 MHz and have performed CW in vivo studies with loop-gap resonators[21,22] and pulsed EPR using a surface coil.[23] The Halpern lab is implementing in vivo imaging at ca. 720 MHz using a permanent magnet to establish the main magnetic field.[24]

In this paper we report the development of a small electromagnet-based 700 MHz imaging system. Important innovations relative to prior 700 MHz spectrometers are the use of rapid scan EPR and a crossed-loop resonator (CLR).[25] In addition, we have designed the system to exploit the capabilities of an arbitrary waveform generator (AWG) to create the excitation and controls for rapid scan imaging and pulsed EPR. The source, bridge and magnet can operate at frequencies between 700 MHz and 1 GHz to permit studies of small animals. The 700 MHz CLR is the only component that would have to be changed to operate at another frequency up to 1 GHz. 2-D and 4-D spectral-spatial RS images of phantoms demonstrate the capabilities of the spectrometer. Pulse experiments were performed to measure magnetic field uniformity and the spin echo dephasing time constant, T_m, of 0.5 mM aqueous trityl-CD_3.

2. System Design

The 700 MHz table-top imaging system block diagram is shown in Figure 1. The radio frequency (RF) source is an 8-bit Tektronix 70002A AWG with a clock speed of 8 Gs/s that can generate waveforms with frequencies up to 1.6 GHz. It has two independent 8-bit RF output channels and four independent 1-bit marker outputs. Although the two RF channels and four markers can be programmed independently, they are phase-locked and derived from a single clock. The marker outputs, used as trigger signals, are routed through a locally constructed TTL converter to boost the voltage from 1 V to 2.75 V peak to peak. The AWG output is approximately −2 dB_m in each channel. For rapid scan operation, the internal sinusoidal function of the AWG supplies the RF waveform. The rapid scan coil driver[26,27] supplies the trigger to the Bruker BioSpin signal processing unit (SPU, part number E5004000) that is used as the digitizer. Commands are sent remotely over RS232 to the coil driver from the PC using a locally written Python program. For pulse experiments, a locally written Matlab program supplies the waveform and marker data to the AWG. For low-power pulse operation the configuration is the same as for rapid scan with the exception that two markers are used to trigger the digitizer and activate the blanking switch that protects the detection system. When used in high power pulse mode, the path shown in the dotted box is used. To switch between rapid scan and high power pulse operation the A2 amplifier (Figure 2) is replaced by the Tomco pulse amplifier, preceded by 23 dB of additional attenuation to keep the Tomco input power at or below 1 mW. The Tomco pulse amplifier nominally outputs 300 W from 400 MHz to 1 GHz and a third marker is used to gate the Tomco pulses. The PC uses the Bruker Xepr data acquisition software, enhanced with locally-written python routines. The power supplies that control the magnetic field and gradients are controlled via Ethernet and synchronized with the data acquisition software via python.

Author Manuscript Author Manuscript Author Manuscript Author Manuscript

3. RF Bridge

Figure 2 shows the block diagram of the locally designed and built bridge. A list of components is in Table 1. Components were selected to have at least 300 MHz bandwidth, centered at about 850 MHz, to permit operation between 700 MHz and 1 GHz. The bridge was designed to operate with a CLR, but with the addition of an external circulator (C1), it can also be used with a reflection loop gap resonator (LGR).

3.1 Resonator Tuning Paths

When the bridge is used with a CLR each resonator, designated CLR 1 and CLR 2, must be tuned individually as well as the isolation between them. To accomplish this a combination of couplers, electronic and mechanical switches are used to route the signals. The tuning paths were designed to be as similar as possible to the operation paths to avoid changes in resonator coupling between tune and operate modes. The switching logic for tuning and operating paths is shown in Table 2 and Figure 3. When tuning either resonator or adjusting isolation, only AWG channel one is used. A reference arm signal is not needed during tuning because the reflected response from the resonator is detected at the operating frequency, without mixing down to DC. A chirp waveform generated by the AWG sweeps RF frequencies encompassing the resonator frequency range. A transfer switch (TS1) directs the signal to the scope monitor output on the back of the bridge, which is connected to a high-speed oscilloscope such as a Lecroy WaveRunner 640Zi. In isolation adjustment mode, the CLR is adjusted to minimize the amplitude of the transmitted signal from the chirp waveform at the resonator frequency, which is a measure of the leakage between CLR 1 and CLR 2. The best possible isolation is important for reducing source noise in rapid scan experiments and resonator ring down in pulse experiments. When the bridge is used with a standard reflection LGR the isolation path is used for tuning. In this path the external circulator (C1) has high isolation, which prevents the RF from being reflected back from port 2 to port 1 of the circulator (see ‘alternate connection’ pathway in Figure 2).

3.2 Operation

The RF from AWG channel one is transmitted through a series of amplifiers, switches and attenuators before reaching the resonator. The maximum RF power at the resonator in CW and low power pulse configuration is 320 mW. The EPR signal from the resonator goes to a locally built quadrature mixer. The AWG channel two output is routed to a voltage-controlled phase shifter (PH1) that provides the reference arm signal for the mixer. The EPR signal is mixed to DC and the quadrature data (I and Q channels) are sent to the locally built video amplifiers. There are three selectable gain settings for the video amplifiers: +20, +30, and +40 dB. A circuit diagram for one channel of the video amplifiers is shown in Figure 4. The gain frequency response is shown in Figure 5 for the I channel. The −3dB bandwidths of the amplifiers are 2.4 ± 0.1, 2.4 ± 0.1 and 2.3 ± 0.1 MHz for 20, 30 and 40 dB gain, respectively. The two channels differ by less than 3%. After the video amplifiers, the signals are routed to the Bruker SPU digitizer for further data analysis.

Author Manuscript Author Manuscript Author Manuscript Author Manuscript

3.3 Noise Figure and Gain Measurement

The noise figure (NF) for the I and Q channels of the video amplifiers was measured using a Fluke 8922A true RMS voltmeter with a sensitivity of −65 dB_m. The measurement was made at +40 dB gain because at lower gains the output noise is below the sensitivity of the true RMS voltmeter. The I-channel has a noise figure of 15.4 dB, and the Q-channel has a noise figure of 15.9 dB. The end-to-end overall gain and NF of the detection system were measured at 700 MHz using the +40 dB video gain setting and the procedure described in Ref. [28,29]. A 32.4 dB calibrated noise source was connected in place of CLR 2 and the noise was measured at the output of the video amplifiers. The measured NF and gain of the I channel were 11.2 ± 0.7 dB and 48.9 ± 0.1 dB, respectively.

The system can be modeled using the Friis equation for cascading amplifiers, given in Ref. 29. Four terms are used to model the system. Two terms represent the first and second stage amplifiers, respectively. The first stage amplifier, A4, has +20.98 dB gain and 0.4 dB NF. The second stage is the video amplifiers with +40 dB gain and 15.4 dB NF. Two additional terms are used in the Friis equation to account for losses in the system. Loss was measured by observing the peak to peak voltage on a 50-ohm scope before and after each component in the system. A total loss of −6.7 dB was measured from the resonator to the first amplifier, A4. An additional loss of −1 dB was measured between A4 and the 0° splitter leading into the quad mixer. There is an estimated total loss of −4.5 dB originating from the splitter and mixer amounting to a total loss of −5.5 dB. When these gains and NFs, summarized in Table 3, are inserted into the Friis equation, a total NF of 9.9 dB is calculated, which is in reasonable agreement with the measured value of 11.2 dB.

4. AWG Programming

The programmability of the AWG allows for a variety of experiments to be performed on the same instrument.

4.1 Continuous RF Output

To generate continuous RF, the greatest common divisor (GCD) between the operating frequency and the clock speed of the AWG is used to calculate the minimum number of points in one waveform, which is needed to ensure that the waveform begins and ends at exactly the same phase.[30] If the waveform does not begin and end at the same phase there is a discontinuity that contributes to source phase noise. The impact on phase noise of the GCD method can be seen in the measured source noise plots in Figure 6. Phase noise is less of a problem when using a CLR than with a LGR because of the isolation between the driven and sample resonators.[31] When the AWG is programmed in this way, and the CLR is used, the source noise is comparable to that of a Fluke 6082A source that we have previously found to work well at 1 GHz.[32] In other tests at X-band the source noise of an AWG was substantially improved by using a Wenzel 500–29237C ‘golden’ clock to drive the AWG clock.[33] At 700 MHz the addition of the Wenzel clock did not substantially change the source noise observed with the CLR. Two-dimensional spectral-spatial images were collected using the Wenzel clock to achieve the highest possible signal to noise. Pulse data were collected using the AWG internal clock and GCD method to calculate the waveform However, any of the

Author Manuscript Author Manuscript Author Manuscript Author Manuscript

configurations could have been used to collect the pulse data without degrading the signal to noise because the source power is off during data acquisition. The four-dimensional spectral-spatial image was collected prior to adding the Wenzel clock so data for that image were obtained using the internal AWG clock without the GCD method. The signal to noise of individual projections could be improved by using the GCD method and the Wenzel clock, but the signal to noise was adequate to perform image reconstruction. The image of the nitroxide was reconstructed in three pieces and the final image is the sum of three images which also increases signal to noise.

4.2 Tuning Waveform

To tune a resonator, a chirp waveform calculated using equation (1) is generated.

$$WF = \sin\left(2\pi\left(f_1 t + \frac{k}{2}t^2\right)\right) \quad (1)$$

where $k = \frac{f_2 - f_1}{T}$, f_1 = starting frequency, f_2 = ending frequency.

The starting and ending frequencies of the waveform are 400 and 900 MHz, respectively. The chirp lasts 70 ms. This waveform is sent through either tuning path 1 or 2 of the bridge. The reflected output is digitized with a Lecroy WaveRunner 640Zi scope digitizing at 10 Gs/s with a 50 ohm load input. The AWG has four independent 1-bit markers any of which can be used to generate a trigger for the scope. The FFT of the reflected signal is computed directly in the scope, which generates a network analyzer type display for tuning.

4.3 Pulse Operation

Pulsed RF waveforms were generated using locally written Matlab programs. Pulse experiments with powers below 300 mW were performed to measure the magnetic field uniformity. High power was not needed for these experiments because the measurements were made with a 2 mm reflection resonator pictured in Figure 7. High power pulse experiments were performed with the 25 mm diameter CLR, which needs more power to create a short 90^o pulse.

5. Magnet, gradients, and power supplies

5.1 CAEN power supplies

Four CAEN Technologies power supplies are used for the magnet and gradient system. The main magnet is powered by a FAST-PS 0540–200 supply. The Z gradient coils are powered by a FAST-PS 1020–200 supply. The X and Y gradient coils are each powered by a FAST-PS 2020–400 supply. Each unit is in a 19-inch 1U box which makes the set very compact. When rack mounted, the four supplies have a combined height of 7 inches. Power supplies are operated in constant current mode with 18-bit current setting resolution. To assess the stability of the main magnet power supply (FAST-PS 0540–200), repeated pulse measurements of a large deoxygenated LiPc sample (1.1 mm inner diameter (ID) x 2 mm long) were made with a small number of averages. The FFT of the free induction decay

Author Manuscript Author Manuscript Author Manuscript Author Manuscript

(FID) has a well-defined peak in the frequency domain that can be converted to field units. The repeatability of this field measurement over time is a measure of power supply stability. A shot repetition time of 100 μs was used so that the total acquisition time for each block of averages was 10 ms. Twenty successive measurements were taken. The standard deviation of the field measured immediately after turning on the system and after 30 min warmup were ± 7 mG (28 ppm) and ± 1 mG (4 ppm), respectively.

5.2 Magnet

Figures 8 and 9 show the magnet and gradient coil assemblies. The magnet coils have 24 turns per layer and 20 layers of No 14-square magnet wire, resulting in a winding cross-section of approximately 1.6 by 1.6 in. (4.1 by 4.1 cm). The two large coils have an average diameter of 7.5 in. (19.1 cm) and are spaced, center-to center, 2.25 in. (5.7 cm). The two small coils have an average diameter of 5.8 in. (14.7 cm) and are spaced, center-to-center, 6.75 in. (17.1 cm). Magnet and gradient coils are potted in Duropot 865 thermally conductive epoxy. The four-coil, uniform field magnet, with the same number of turns on each coil, was derived by Braunbeck[34] when the windings are small compared to coil diameter. The object of the magnet design was to provide a uniform field with minimum power, which requires windings with a large cross-section relative to coil diameter. The design of this type magnet, for this case, is given by Garrett.[35] The magnet coil constant is 78.5 Gauss/Amp. The resistance of the four coils in series is 7 Ohms. Therefore, for 250 Gauss (700 MHz), the magnet power is 71 Watts, which permits air cooling.

5.3 Z-Gradient Coils

The Z-direction is along the axis of magnet. The Z-gradient coil is a system based on the design from Maxwell,[36] which is also given by Garrett.[35] The Z-coils are concentric with and located inside the large magnet coils. The inside diameter of the Z-coils is the same as the small magnet coils. The outside diameter is slightly less than the inside diameter of the large magnet coils. The Z-coils have 12 turns per layer and 7 layers of No 10 wire. Each Z-gradient coil has an average diameter of about 5.2 in. (13.2 cm). The coil cross-section is 1.3 by 0.74 in. (3.3 by 1.9 cm). The Z-gradient coil constant is 1.88 Gauss/cm-Amp, and consumes about 8 Watt at 10 Gauss/cm.

5.4 X-, Y- Gradient Coil Assembly

The X-, Y-gradient coils assembly is shown in Figure 9. Each of these gradient coils consists of two layers of Golay type coils.[37] Each coil has two layers, with 10 turns of No. 14 square magnet wire per layer. The average diameter of the X-gradient Golay assembly is 4.1 in. (10.4 cm) and the average diameter of the Y-gradient, Golay assembly is 3.82 in. (9.7 cm). The gap between the coils is 0.75 in. (1.9 cm) and the overall length of the assembly is 7.5 inches. The assembly is epoxied to two fiberglass coil supports as shown in the Figure 9, leaving the gap unobstructed at the top for access to tune the resonator. The coil constant for the X-gradient coil is 0.74 Gauss/cm-Amp and the coil consumes 51 Watt at 10 Gauss/cm. The coil constant for the Y-gradient coil is 0.8 Gauss/cm-Amp and the coil consumes 35 Watts at 10 Gauss/cm. The X-, Y-gradient assembly slides inside the small magnet coils and the Z-gradient coils, shown in Figure 8. This arrangement results in a very compact system.

Author Manuscript Author Manuscript Author Manuscript Author Manuscript

5.5 Magnetic Field Uniformity

The theoretical uniformity of the magnet, if all coils are perfectly wound and properly spaced, is 15 ppm over a sphere 2 in. (5 cm) in diameter. The coil positions were set as accurately as possible to theoretical spacings and then refined by making measurements of the B_0 field uniformity. A 2.4 mm ID, 6 mm long reflection resonator was mounted on the end of a ¼ inch square ruler. A positioning system shown in Figure 10 was used to guide the small resonator (Figure 7) to defined positions within the magnet. The structure fits within the gradient coils such that uniformity measurements can be made with or without an applied field gradient. The LiPc sample is the same as was used to measure power supply stability. With the resonator placed approximately in the center of the magnet, a constant B_0 field was set to a value slightly off resonance to generate an FID with strong oscillations. To map the magnetic field the resonator was moved to precise positions within the magnet. The field value at each position was measured by taking the FFT of the FID. The frequency was then converted to magnetic field units as a relative offset from resonance. The actual field value at each position was calculated by adding the static B_0 field to the field offset from resonance. This procedure for measuring local magnetic field is similar to that described in Ref. 38.

Adjustments in the coil spacings were made using a dial indicator. A locally written Mathcad program was used to calculate the necessary adjustments for each coil. The main magnet nonuniformity after best possible adjustment has linear gradients in the X-, Y-, and Z-directions. Appropriate gradients of equal and opposite magnitude can be applied to cancel out the unwanted residual gradient. The final values of nonuniformity over the sample space after corrections are applied are less than 25 ppm as shown in Table 4.

5.6 Gradient Coil Calibration

Gradient coil constants were measured using the same procedure and LiPc sample as described for the homogeneity and stability tests. The sample was placed in a defined spatial location along the X, Y, or Z axes. Gradient currents from 0.1 A to 0.5 A were applied and the FID frequency was recorded for each current value. The sample was then moved a precise distance within the sample space and the FID was remeasured using the same gradient currents. For each position the change in gauss was divided by the known spatial offset. The gradient coil constants were calculated from the slope of a plot of G/cm vs Amp. Small non-zero Y axis intercepts were included as corrections when calculating gradients for the imaging experiment. Calculated values for the X, Y, and Z gradient coil constants are shown in Table 5.

5.7 Magnet Temperature Measurements

The magnet and gradient coils do not require water cooling. Temperature measurements were made at four surface positions on the coils. The magnet was energized to 250 G and all gradient coils were energized to 10 G/cm. A rapid scan field of 60 G was generated. A small fan blowing air along the bore of the magnet keeps the surface temperature below 40 °C after approximately an hour of operation.

Author Manuscript Author Manuscript Author Manuscript Author Manuscript

6. Resonator

The 700 MHz rapid scan CLR is shown in Figure 11. CLR 1 is the driven resonator and CLR 2 is the sample resonator. The two resonators are saddle coils constructed of ¼ in. (6.4mm) wide, adhesive backed, copper foil. The coils are resonated using Voltronics, series 5, nonmagnetic chip capacitors. Both resonators are 1.5 in. (38 mm) long. The sample resonator is mounted on a high impact polystyrene (HIPS) plastic tube, 1.1 in, (28 mm) outer diameter (OD) and 1.03 in. (26 mm) ID and 3.3 in. (84 mm) long. It is attached to a circular RF shield 2.785 in (73 mm) in diameter and 3.3 in. (84 mm) long. The shield is 3-D printed using polylactic acid (PLA) and is coated on the inside with silver paint. The driven resonator is constructed on a HIPS tube 1.3 in. (33 mm) OD and 2.7 in. (69 mm) long and is mounted by bearing surfaces on each end to allow free rotation on its axis. The isolation screw and return spring provide fine adjustment of the axis of the driven resonator to make it, electrically, perpendicular to the axis of the sample resonator. The driven resonator is tuned in frequency using a Johanson 5761 nonmagnetic 0.6 to 6 PF variable capacitor. Both resonators are fixed coupling using chip capacitors and are slightly over-coupled. The efficiency of the driven resonator is approximately 0.11 G/sqrt(W). Critical coupling is not necessary for CLRs since isolation of the source and the detector is achieved by the physical adjustment of the orthogonality of the resonators. The Q of each resonator is about 40 and isolation between them is typically 31 dB. Both resonators are over-coupled when empty. The addition of an aqueous sample brings the coupling closer to critical and also lowers the frequency about 2%.

Figure 12 is an equivalent circuit for the sample resonator (CLR 2). The two saddle coils are connected at the center by a parallel conductor transmission line. These conductors are 3/16 in. (4.8 mm) wide, separated by 0.02 in (0.5 mm). Because of the close spacing and the fact that the current in the conductors is in opposite directions to that in the two loops, the conductors do not contribute significantly to the magnetic field in the resonator. This “cross-over” connection is shown in the center of the diagram in Figure 12. Coupling to the resonator from input A-A’ is via two 1.5 pF chip capacitors. Two capacitors are used in each loop to reduce to possibility of self-loop resonance. The inductance of the loops, based on the resonant frequency and resonant capacitance, is on the order of 10 nH.

Figure 13 is an equivalent circuit for the driven resonator (CLR 1). It is like the sample resonator except that it is about 30% larger and has two cross-over lines. The cross-over in the center of the diagram has a 4.3 pF capacitor in the center and is coupled to A-A’ via two 2.2 pF capacitors. In the center of the second cross-over is a 0.6 – 6 pF variable capacitor for tuning the resonant frequency. The loop inductance of this saddle coil is on the order of 12 to 15 nH. The two cross-overs are the same length, 0.8 in, (20 mm). The long lines at the bottom of the diagram merely show the connection.

The rapid scan coils have 88 turns of 220/46 Litz wire and a coil constant of 15.7 G/A. The trityl-CD_3 ^{13}C hyperfine values are well known and were used to calibrate the rapid scan coil constant.[39] The rapid scan coils have an inductance of 1.9 mH.

Author Manuscript Author Manuscript Author Manuscript Author Manuscript

7. Samples

A 0.1 mM triarylmethyl (OX63) solution was prepared in 2 mM HEPES (4-(2-hydroxyethyl)-1-piperazine-ethanesulfonic acid) buffer. Aqueous solutions of 0.5 mM triarylmethyl (Trityl) CD_3, 1 mM 4-hydroxy-2,2,6,6-tetramethylpiperidin-1-oxyl (Tempol, SigmaAldrich, St. Louis, MO), and ^{15}N per-deuterated Tempone (PDT, Cambridge Isotope Laboratories, Tewksbury, MA) solutions also were prepared. Solution samples were degassed with N_2 and flame sealed. The Lithium phthalocyanine (LiPc) was evacuated on a high vacuum line and flame sealed. Custom made Pyrex flasks were manufactured by Allen Scientific glass in three geometries. The first geometry is a cylinder 25 mm in diameter x 25 mm long (tube **a**). The second geometry is a cylinder 25 mm in diameter x 16 mm long (tube **b**). Another geometry consisted of a half cylinder 25 mm in diameter x 16 mm long (tube **c**). Dimensions are outer diameters. When placed side by side two of these half cylinder flasks have the same diameter as the 25 mm cylinders. The wall thickness of the specially made flasks is approximately 1.5 mm.

8. Experimental Results.

8.1 High Power Pulse

High power pulse experiments using the Tomco amplifier were carried out on a degassed 0.5 mM aqueous 25 mm sample of Trityl-CD_3 (tube **a)**. T_m was measured using a $\pi/2$ and π pulse lengths of 200 and 400 ns, respectively. The echo at each τ value was collected as a transient experiment. In post-processing the maximum amplitude of the echo for each τ value was plotted as a function of 2τ. The echo decay curve (Figure 14) was fit with a single exponential to determine T_m. The average of three measurements was 11.3 ± 0.4 μs which agrees with previous values made at 250 MHz and L-band for this sample.[40]

8.2 Two-Dimensional Spectral-Spatial Imaging

Two-dimensional spectral-spatial images of a phantom (Figure 15B) containing 1 mM Tempol, 1 mM ^{15}N PDT and 0.1 mM OX63 were collected using sinusoidal rapid scans. The phantom consisted of one tube **b** filled with 0.1 mM OX63 and two tube **c**'s containing 1mM ^{14}N Tempol and 1 mM ^{15}N PDT, respectively. The two tube **c**'s were placed side-by-side to form a cylinder. The pair of half cylinders was placed bottom to bottom with the whole cylinder (tube **b**) with the separations between compartments aligned along the X and Z-axes. The rapid scan frequency was 3.133 kHz with a 75 G sweep width. The gradients for the individual images were varied from −10 G/cm to +10 G/cm in 0.1 G/cm steps generating a total of 201 projections. Three rapid scan cycles were collected for each projection and signal was averaged 65534 times. Microwave power was selected such that the OX63 signal amplitude was at least 95% of the value in the absence of saturation. The reconstruction algorithm used is described in Ref. [41]. In Figure 16 the gradient was varied along the x-axis. In Figure 17 the gradient was varied along the z axis. In Figure 16, spectral slices at X= −0.53 cm and X= +0.48 cm are shown. The spatial separation measured along x was approximately 3.7 mm. In Figure 17, spectral slices through Z= −0.85 cm and Z=+0.59 cm are shown. The spatial separation measured along Z was approximately 3.2 mm, which is consistent with twice the wall thickness of 1.5 mm, and imperfect contact between the tubes.

Author Manuscript Author Manuscript Author Manuscript Author Manuscript

The spectral slices agree well with the non-gradient spectrum. In the non-gradient spectrum the line widths of the absorption spectrum measured at full width at half maximum (FWHM) of OX63, Tempol, and ^{15}N PDT were 0.31, 2, and 0.48 G respectively. In the spectral slices from the 2D images the corresponding FWHM linewidths were 0.45, 1.8, and 0.58 G. The discrepancies between linewidths in the images and the non-gradient spectra are attributed to the limited number of projections and the large spectral widths. The spatial resolution of the images is about 0.5 mm.

8.3 Four-Dimensional Spectral-Spatial Imaging

A four-dimensional image in which the fourth dimension is the spectral axis was acquired by sinusoidal rapid scan EPR for a phantom (Figure 15A) consisting of two cylinders (tube **b**). One cylinder contained 0.1 mM OX63 and the other 1 mM ^{14}N Tempol. The two tubes were offset along the z-axis. Microwave power was optimized such that the OX63 signal amplitude was at least 95% of the value in the absence of saturation. The rapid scan frequency was 3.133 kHz and the sweep width was 75 G. The maximum gradient was 10 G/cm. There were 14 spectral projections acquired at each of 10 spatial angles using an equal solid angle sampling scheme for a total of 924 total projections. Three rapid scan cycles were collected for each projection and signal averaged 50,000 times. The projections were deconvolved to yield the slow scan spectrum before image reconstruction. The reconstruction software utilizes a filtered-back projection method.[42,43] The images had 64 bins for the spatial axes. The spatial resolution of the images is about 1.6 mm. The center portion of the spectrum reconstructed both the center line of the nitroxide and the OX63 signal (Figure 18). The image of the nitroxide was reconstructed in three pieces in which each nitrogen hyperfine line was reconstructed individually. The nitroxide image (Figure 19) is the sum of the separate images for the three hyperfine lines. The locations and lineshapes of EPR signals in the image are in good agreement with the known characteristics of the phantom. The measured spatial separation between the two cylinders along Z was approximately 3.2 mm. To display the spectral dimension three slices at adjacent steps along the Z axis that correspond to the nitroxide and OX63 compartments, respectively, were summed. There are 64 points along the spectral axis so the OX63 lineshape is defined by only a few points.

9. Discussion

The spectrometer described in this paper can be used to perform both rapid scan and pulse EPR experiments at 700 MHz. The electronics and magnet can operate at frequencies at 700 MHz to 1 GHz. The versatility of the AWG makes this flexibility possible. We have shown that at 700 MHz, using a CLR, phase noise from the AWG is comparable to other “gold standard” RF sources. The operating frequency of 700 MHz was chosen to facilitate improved signal to noise relative to 250 MHz while still maintaining adequate depth of penetration for imaging experiments. Smaller spectrometers are the future of pre-clinical imaging applications. This table-top magnet design does not require water cooling and is a step towards a pre-clinical imager. Future directions include implementing 1 GHz imaging. The step from 700 MHz to 1 GHz is non-trivial when the resonator is as large as 25 mm

Author Manuscript Author Manuscript Author Manuscript Author Manuscript

diameter; the resonator becomes more sample dependent. Experience with a 25 mm diameter, 1 GHz CLR will be described in a future paper.

Acknowledgements

Funding for this work from National Institutes of Health P41 EB002034 (H. J. Halpern, PI) and R01CA177744 (GRE, PI) is gratefully acknowledged. Boris Epel provided guidance for reconstruction of the 4D image. Examples provided at http://epr-it.specman4epr.com/ were used as a starting point for the reconstruction. The samples of trityl-CD_3 and OX63 were gifts from Prof. Howard Halpern (University of Chicago). LiPc was provided by Prof. Harold M. Swartz (Dartmouth University).

References

1. Epel B, Sundramoorthy SV, Krzykowska-Serda M, Maggio MC, Tseytlin M, Eaton GR, Eaton SS, Rosen GM, Kao JPY, Halpern HJ. 2017 Imaging Thiol Redox Status in Murine Tumors In Vivo with Rapid-scan Electron Paramagnetic Resonance. J. Magn. Reson 276:31–36 [PubMed: 28092786]
2. Epel B, Haney CR, Hleihel D, Wardrip C, Barth ED, Halpern HJ. 2010 Electron paramagnetic resonance oxygen imaging of a rabbit tumor using localized spin probe delivery. Med. Phys 37:2553–2559. [PubMed: 20632567]
3. Swartz HM, Khan N, Khramtsov VV. 2007 Use of electron paramagnetic resonance spectroscopy to evaluate the redox state in vivo Antioxidants & Redox Signaling 9:1757–1771. [PubMed: 17678441]
4. Halpern HJ. 2003 Stable soluble paramagnetic compounds. Biol. Magn. Reson 18:201–232.
5. Kuppusamy P, Li H, Ilangovan G, Cardounel AJ, Zweier JL, Yamanda K, Krishna MC, Mitchell JB. 2002 Noninvasive imaging of tumor redox status and its modification by tissue glutathione levels. Cancer Res. 62:307–312. [PubMed: 11782393]
6. Halpern HJ, Yu C, Peric M, Barth E, Grdina DJ, Teicher BA. 1994 Oxymetry deep in tissues with low-frequency electron paramagnetic resonance. Proc. Natl. Acad. Sci. U. S 91:13047–51.
7. Bobko AA, Eubank TD, Voorhees JL, Efimova OV, Kirilyuk IA, Petryakov S, Trofimiov DG, Marsh CB, Zweier JL, Grigorev IA and others. 2012 In Vivo Monitoring of pH, Redox Status, and Glutathione Using L-Band EPR for Assessment of Therapeutic Effectiveness in Solid Tumors. Magn. Reson. Med 67:1827–1836. [PubMed: 22113626]
8. Khramtsov VV, Weiner LM, Grigoriev IA, Volodarsky LB. 1982 Proton exchange in stable nitroxyl radicals. EPR study of the pH of aqueous solutions. Chem. Phys. Lett 91:69–72.
9. Biller JR, Tseitlin M, Quine RW, Rinard GA, Weismiller HA, Elajaili H, Rosen GM, Kao JP, Eaton SS, Eaton GR. 2014 Imaging of Nitroxides at 250 MHz using Rapid-Scan Electron Paramagnetic Resonance. J. Magn. Reson 242:162–168. [PubMed: 24650729]
10. Eaton SS, Shi Y, Woodcock L, Buchanan LA, McPeak J, Quine RW, Rinard GA, Epel B, Halpern HJ, Eaton GR. 2017 Rapid Scan EPR Imaging. J. Magn. Reson 280 140–148. [PubMed: 28579099]
11. Rinard GA, Quine RW, Eaton SS, Eaton GR. 2004 Frequency dependence of EPR sensitivity. Biol. Magn. Reson 21:115–154.
12. Gorter CJ. Paramagnetic Relaxation. Amsterdam: Elsevier Publishing Co.; 1947.
13. Shi Y, Quine RW, Rinard GA, Buchanan L, Eaton SS, Eaton GR, Epel B, Seagle SW, Halpern HJ. 2017 Triarylmethyl Radical: EPR Signal to Noise at Frequencies between 250 MHz and 1.5 GHz and Dependence of Relaxation on Radical and Salt Concentration and on Frequency Z. Physik. Chem 231:923–937.
14. Shi Y, Quine RW, Rinard GA, Buchanan L, Eaton SS, Eaton GR, Epel B, Seagle SW, Halpern HJ. 2017 Triarylmethyl Radical OX063d24 Oximetry: Electron Spin Relaxation at 250 MHz and RF Frequency Dependence of Relaxation and Signal-to-Noise. Adv. Exp. Med. Biol 977:327–334. [PubMed: 28685462]
15. Halpern HJ, Bowman MK. Low-frequency EPR spectrometers: MHz range In: Eaton GR, Eaton SS, Ohno K, editors. EPR Imaging and In Vivo EPR. Boca Raton: CRC Press; 1991 p ch. 6.

Author Manuscript Author Manuscript Author Manuscript Author Manuscript

16. Halpern HJ, Spencer DP, van Polen J, Bowman MK, Nelson AC, Dowey EM, Teicher BA. 1989 Imaging radio frequency electron-spin-resonance spectrometer with high resolution and sensitivity for in vivo measurements. Rev. Sci. Instrum 60:1040–1050.
17. Murugesan R, Afeworki M, Cook JA, Devasahayam N, Tschudin R, Mitchell JB, Subramanian S, Krishna MC. 1998 A broadband pulsed radio frequency electron paramagnetic resonance spectrometer for biological applications. Rev. Sci. Instrum 69:1869–1876.
18. Eaton SS, Eaton GR. 2004 EPR at frequencies below X-band. Biol. Magn. Reson 21:59–114.
19. Takeshita K, Ozawa T. 2004 Recent progress in in vivo ESR spectroscopy. J. Radiat. Res 45:373–384. [PubMed: 15613782]
20. Han JY, Hong JT, Oh K-W. 2010 In vivo electron spin resonance: an effective new tool for reactive oxygen species/reactive nitrogen species measurement. Arch. Pharm. Res 33:1293–1299. [PubMed: 20945126]
21. Ito T, Yokoyama H, Sato T, Ogata T. 2001 Influence of the lens effect in a sample with large dielectric constant in a loop-gap resonator on the EPR signal intensity at 700 MHz. Appl. Magn. Reson 21:97–103.
22. Sato T, Yokoyama H, Ohya H, Kamada H. 2002 An active resonator system for CW-ESR measurement operating at 700 MHz. J. Magn. Reson 159:161–166.
23. Matsumoto S, Espey MG, Utsumi H, Devasahayam N, Matsumoto K-I, Matsumoto A, Hirata H, Wink DA, Kuppusamy P, Subramanian S and others. 2008 Dynamic monitoring of localized tumor oxygenation changes using RF pulsed electron paramagnetic resonance in conscious mice. Magn. Reson. Med 59:616–625.
24. Halpern HJ. personal communication. 2018.
25. Rinard GA, Quine RW, Ghim BT, Eaton SS, Eaton GR. 1996 Dispersion and superheterodyne EPR using a bimodal resonator. J. Magn. Reson. A 122(1):58–63.
26. Quine RW, Czechowski T, Eaton GR. 2009 A Linear Magnetic Field Scan Driver. Conc. Magn. Reson., Magn. Reson. Engineer 35B:44–58.
27. Quine RW, Mitchell DG, Eaton SS, Eaton GR. 2012 A Resonated Coil Driver for Rapid Scan EPR. Conc. Magn. Reson., Magn. Reson. Engineer 41B:95–110.
28. Keysight High Accuracy Noise Figure Measurements Using the PNA-X Series Network Analyzer. In: Keysight, editor. literature.cdn.keysight.com/litweb/pdf/5990-5800EN.pdf. Volume 5990–5800EN; 2014 p 7.
29. Rinard GA, Quine RW, Song R, Eaton GR, Eaton SS. 1999 Absolute EPR Spin Echo and Noise Intensities. J. Magn. Reson 140(1):69–83. [PubMed: 10479550]
30. Byrom B personal communication from Tektronix representative. 2017.
31. Rinard GA, Quine RW, Biller JR, Eaton GR. 2010 A Wire Crossed-Loop-Resonator for Rapid Scan EPR. Concepts Magn. Reson. B, Magn. Reson. Engineer 37B:86–91.
32. Quine RW, Rinard GA, Ghim BT, Eaton SS, Eaton GR. 1996 A 1–2 GHz pulsed and continuous wave electron paramagnetic resonance spectrometer. Rev. Sci. Instrum 67(7):2514–2527.
33. McPeak JE, Quine RW, Eaton SS, Eaton GR. 2018 An X-band Saturation Recovery EPR Spectrometer Based on an Arbitrary Waveform Generator. Rev. Sci. Instrum submitted for publication.
34. Braunbeck W 1934 Die Erzeugung Weitgehend Homogener Magnetfelder Durch Kreisströme. Zeit. für Physik 88:399–402.
35. Garrett MW. 1967 Cylindrical coil systems for strong magnetic field or gradient homogeneities of the 6th to 20th order. J. Appl. Phys 38:2563–2586.
36. Maxwell JC. Treatise on Electricity and Magnetism, Oxford: The Clarendon Press; 1873.
37. Siebold H 1990 Gradient Field Coils for MR Imaging with High Spectral Purity. Transactions on Magnetics 26:897–900.
38. Sundramoorthy SV, Epel B, Halpern HJ. 2017 A Pulse EPR 25 mT Magnetometer with 10 ppm Resolution. Appl. Magn. Reson 48:805–811. [PubMed: 29151678]
39. Trukhan SN, Yudanov VF, Rogozhnikova O, Trukhin D, Bowman MK, Krzyaniak MD, Chen H, Martyanov ON. 2013 Hyperfine Interactions of Narrow-line Trityl Radicals with Solvent Molecules. J. Magn. Reson 233:29–36. [PubMed: 23722184]

Author Manuscript Author Manuscript Author Manuscript Author Manuscript

40. Owenius R, Eaton GR, Eaton SS. 2005 Frequency (250 MHz to 9.2 GHz) and Viscosity Dependence of Electron Spin Relaxation of Triarylmethyl Radicals at Room Temperature. J. Magn. Reson 172:168–175. [PubMed: 15589420]

41. Tseitlin M, Biller JR, Elajaili H, Khramtsov V, Dhimitruka I, Eaton GR, Eaton SS. 2014 New spectral-spatial imaging algorithm for full EPR spectra of multiline nitroxides and pH sensitive trityl radicals. J. Magn. Reson 245:150–155. [PubMed: 25058914]

42. Ahn K-H, Halpern HJ. 2007 Spatially uniform sampling in 4-D EPR spectral-spatial imaging. J. Magn. Res 185:152–158.

43. Qiao Z, Redler G, Gui Z, Qian Y, Epel B. 2018 Three novel accurate pixel-driven projection methods for 2D CT and 3D EPR Imaging. J. Xray Sci. Tech 26:83–102.

Author Manuscript Author Manuscript Author Manuscript Author Manuscript

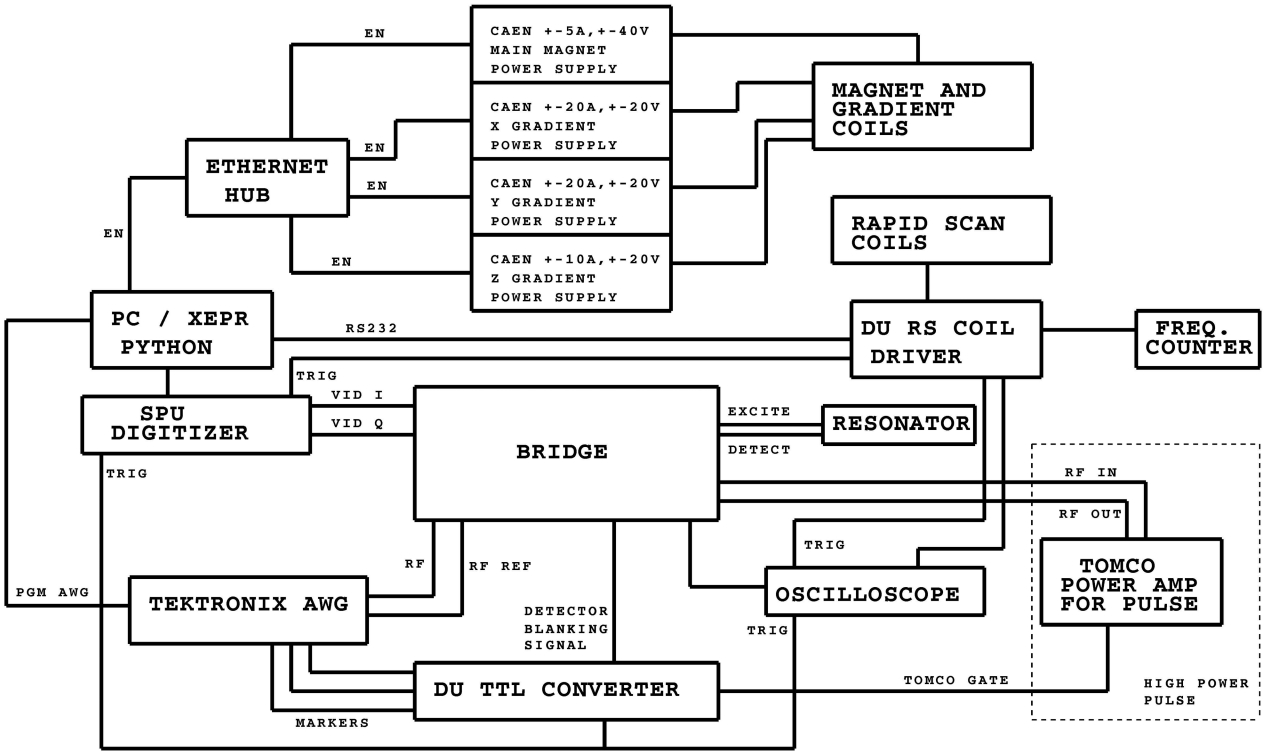

EN = ETHERNET
TRIG = TRIGGER
VID = VIDEO

Figure 1.
Block diagram of the rapid scan and pulse system.

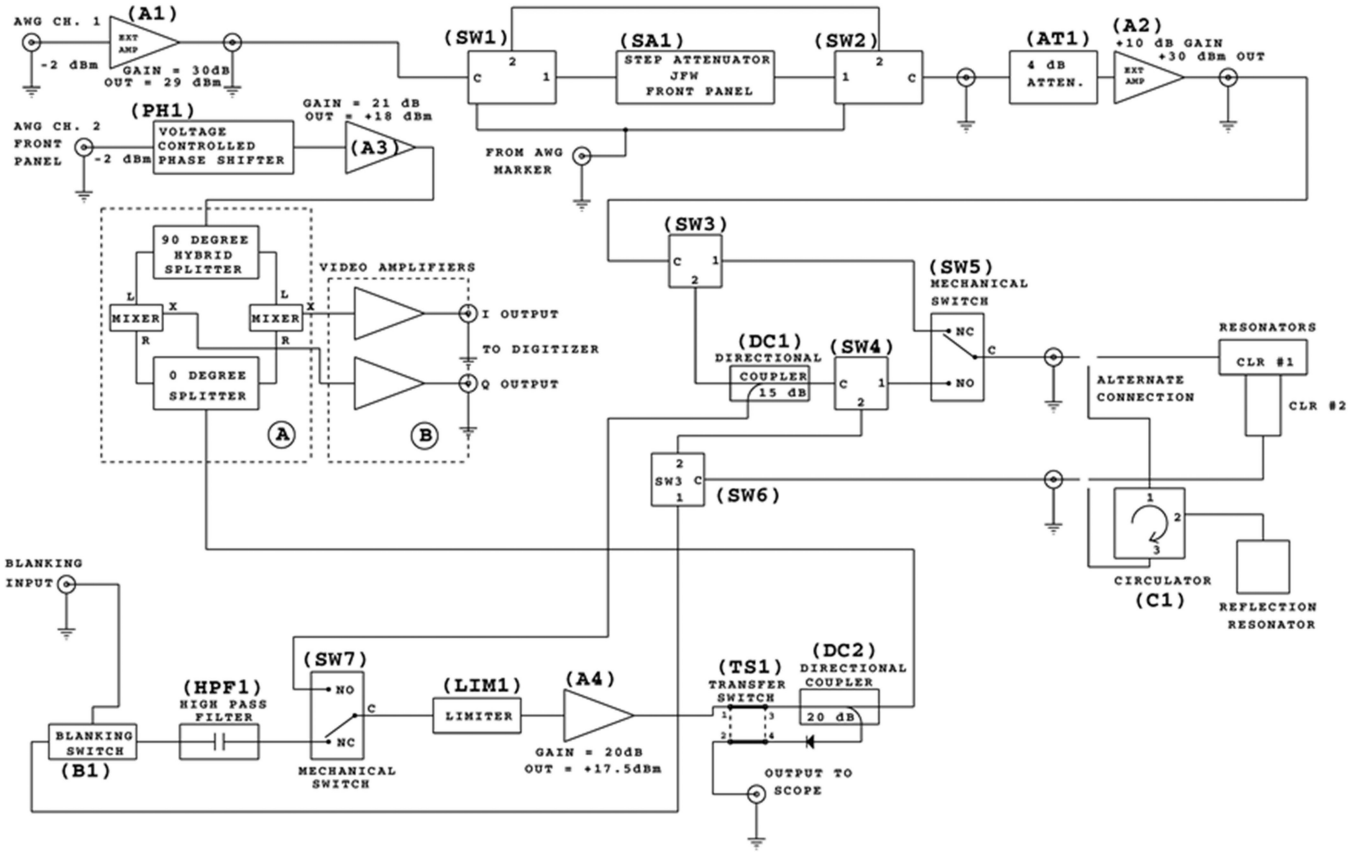

Figure 2.

Block diagram of bridge. The mechanical switches are shown in the normally closed (NC) positions, which is the path for operation rather than tuning.

Author Manuscript Author Manuscript Author Manuscript Author Manuscript

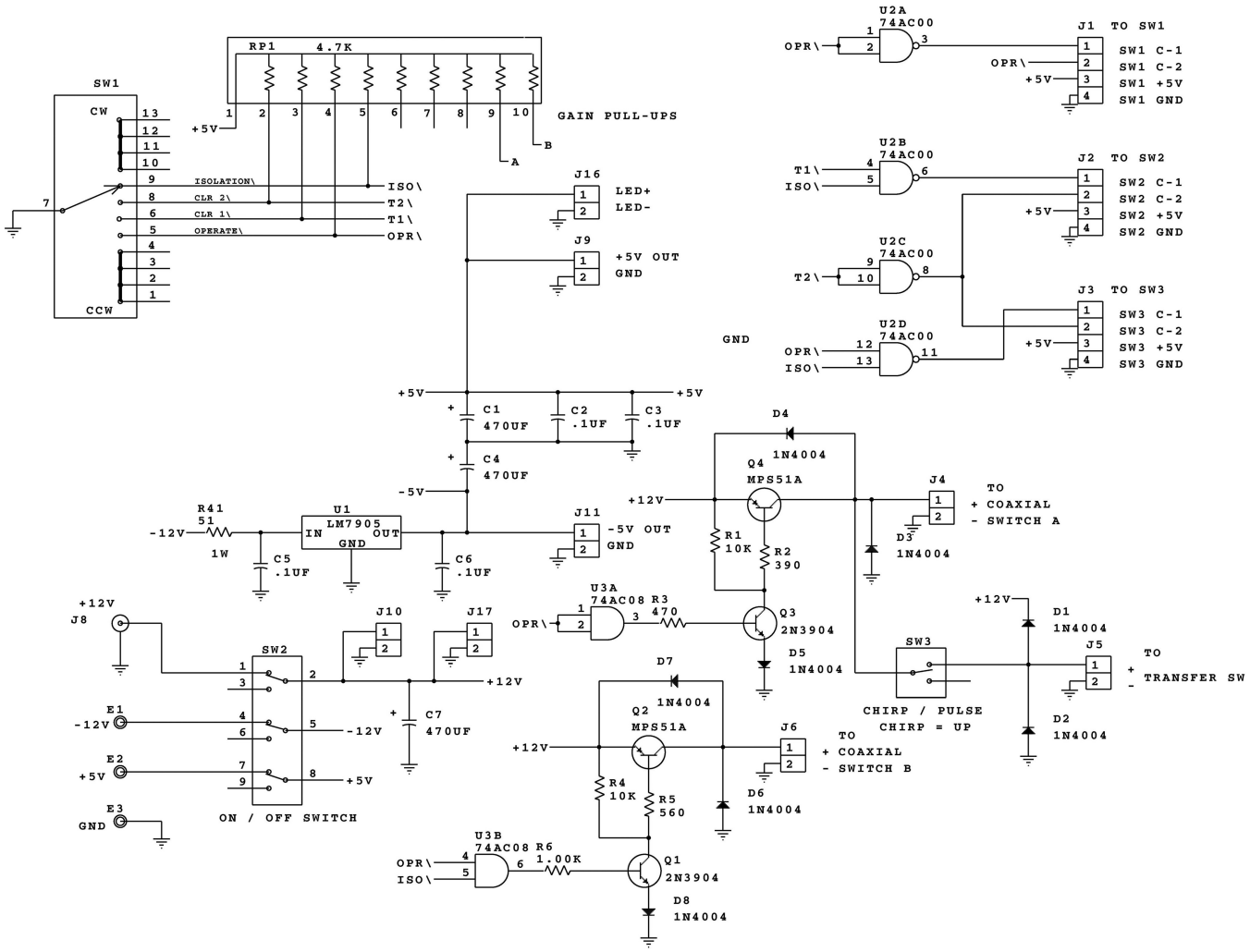

Figure 3.
Switching logic for bridge.

Author Manuscript Author Manuscript Author Manuscript Author Manuscript

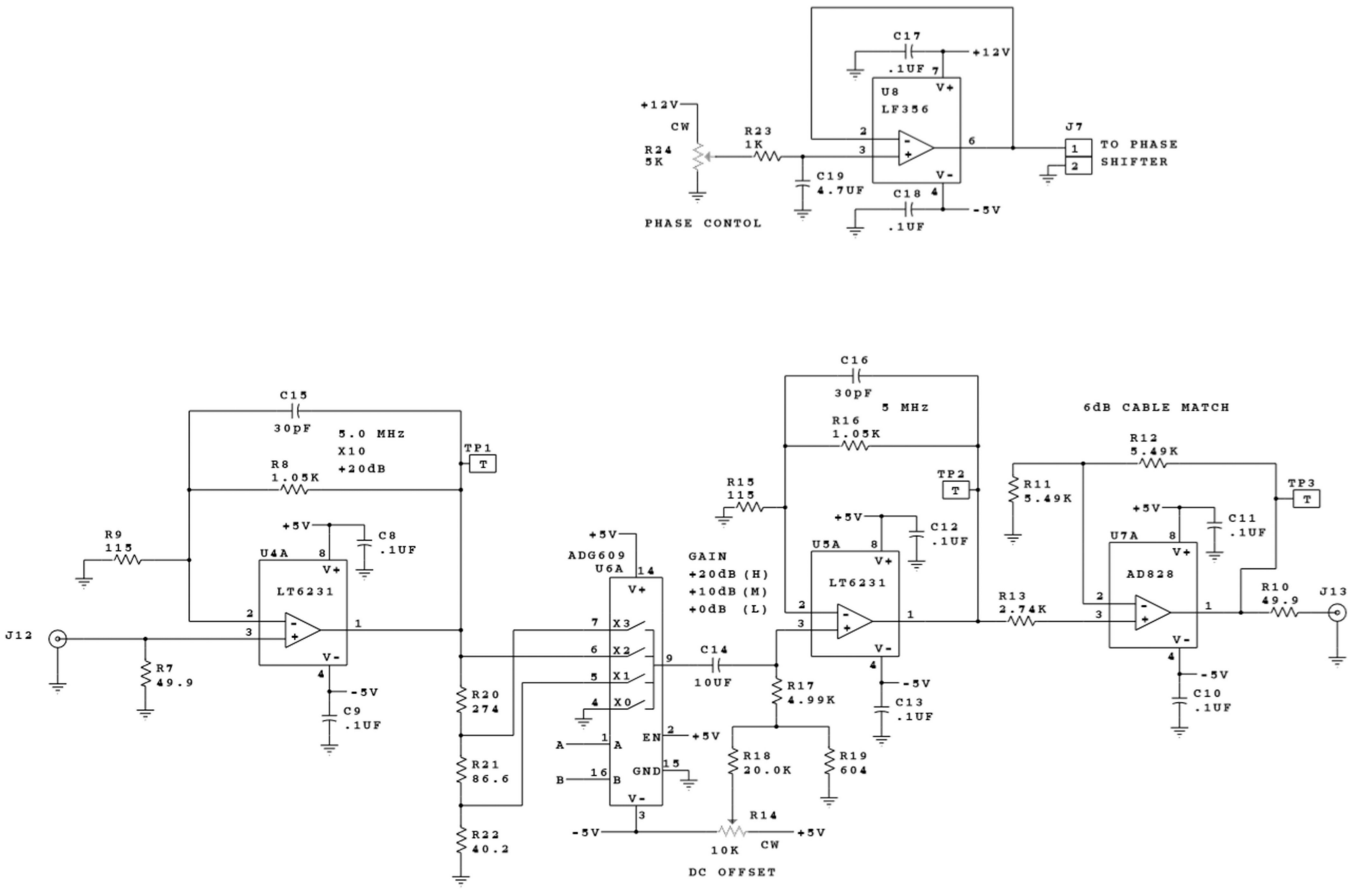

Figure 4.

One channel of the video amplifiers and the phase control circuit.

Author Manuscript Author Manuscript Author Manuscript Author Manuscript

Author Manuscript Author Manuscript Author Manuscript Author Manuscript

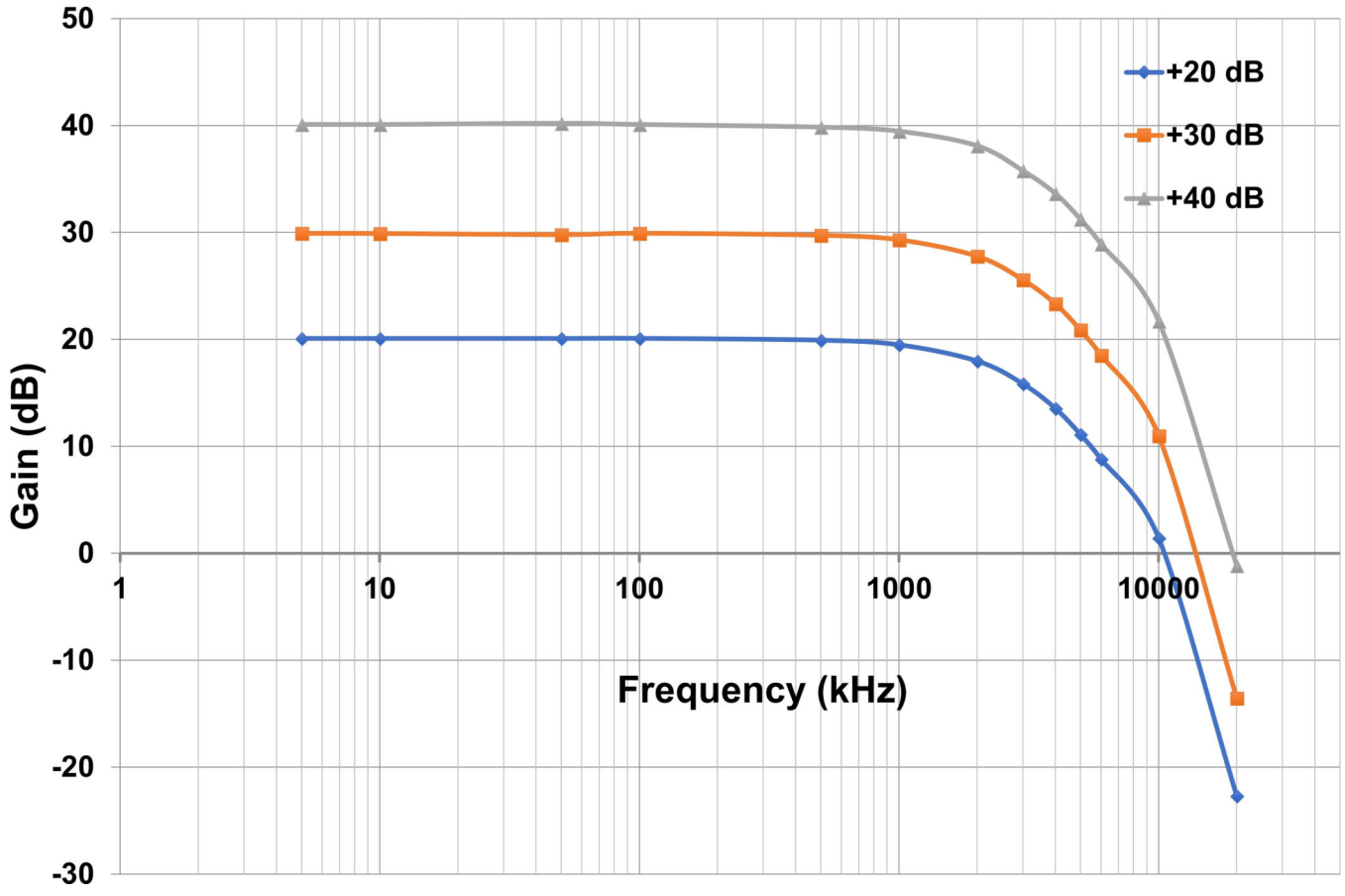

Figure 5.
Gain vs. Frequency for one channel of the video amplifiers.

Author Manuscript Author Manuscript Author Manuscript Author Manuscript

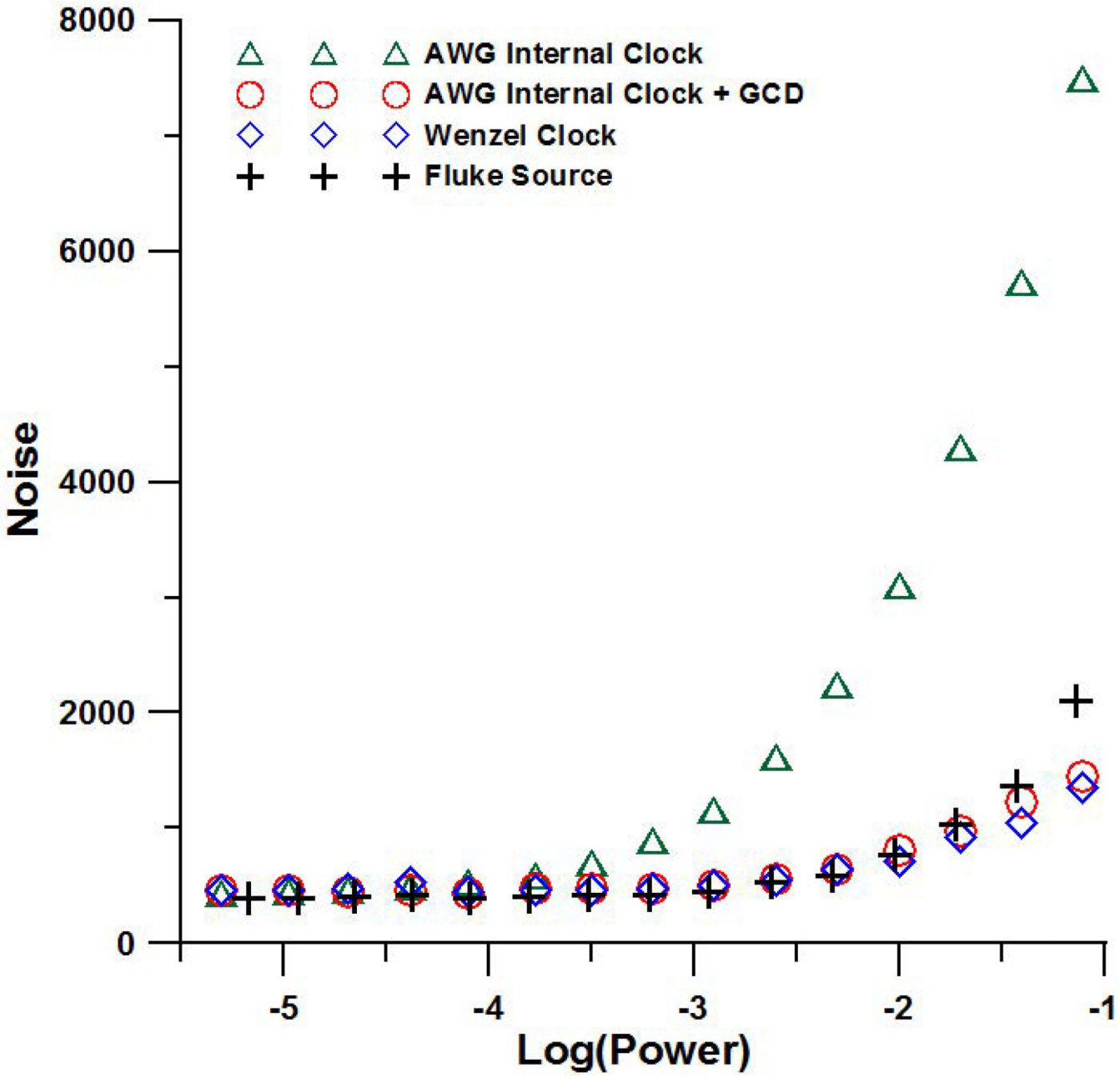

Figure 6.
Source noise of various sources as a function of power incident on the resonator.

Author Manuscript Author Manuscript Author Manuscript Author Manuscript

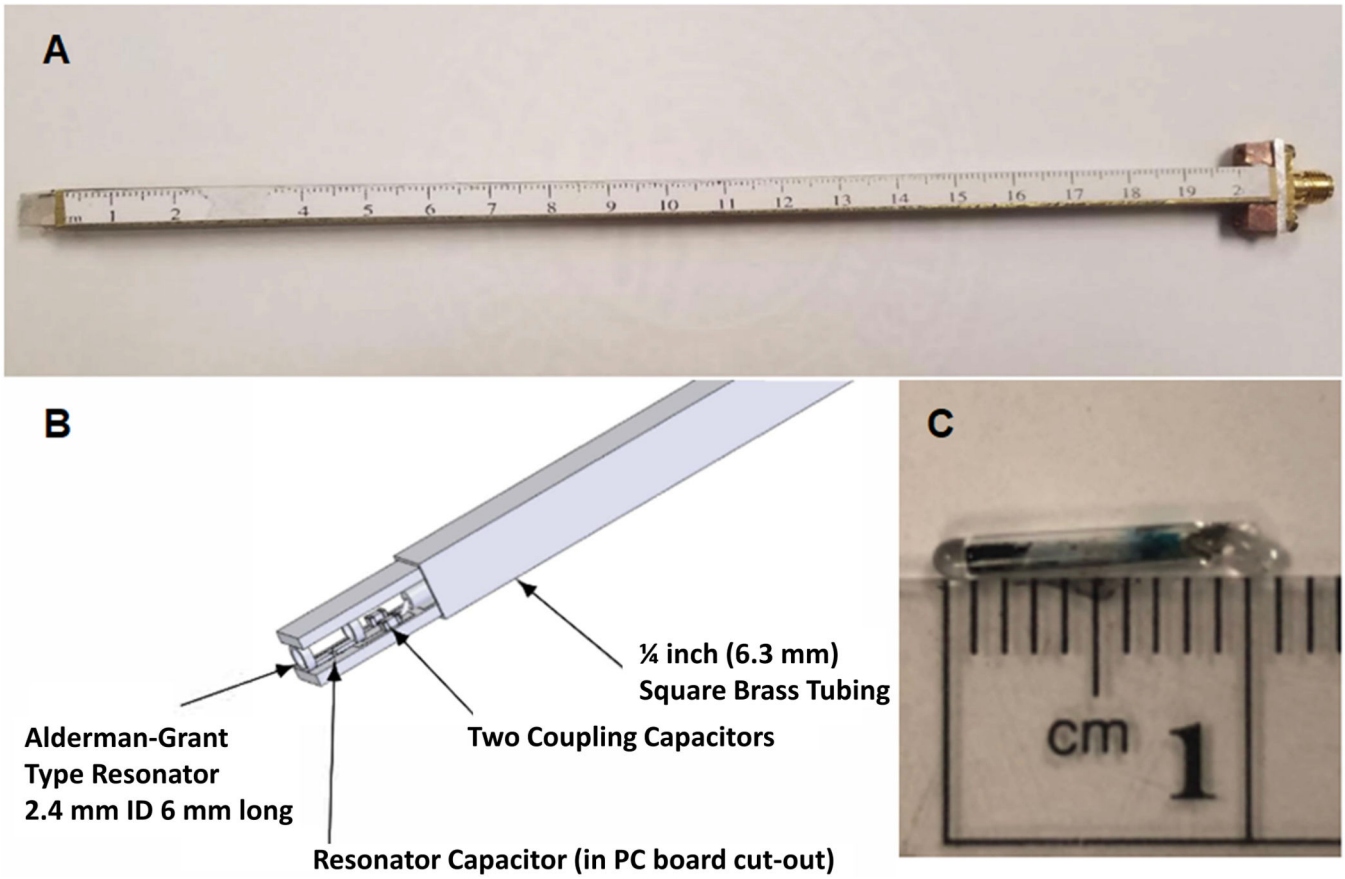

Figure 7.

(A) Picture of reflection resonator assembly used to probe magnetic field uniformity. (B) Sketch of field probe pictured in part A. **(**C) 2 mm LiPc sample used to measure magnetic field uniformity and gradient coil constants.

Author Manuscript Author Manuscript Author Manuscript Author Manuscript

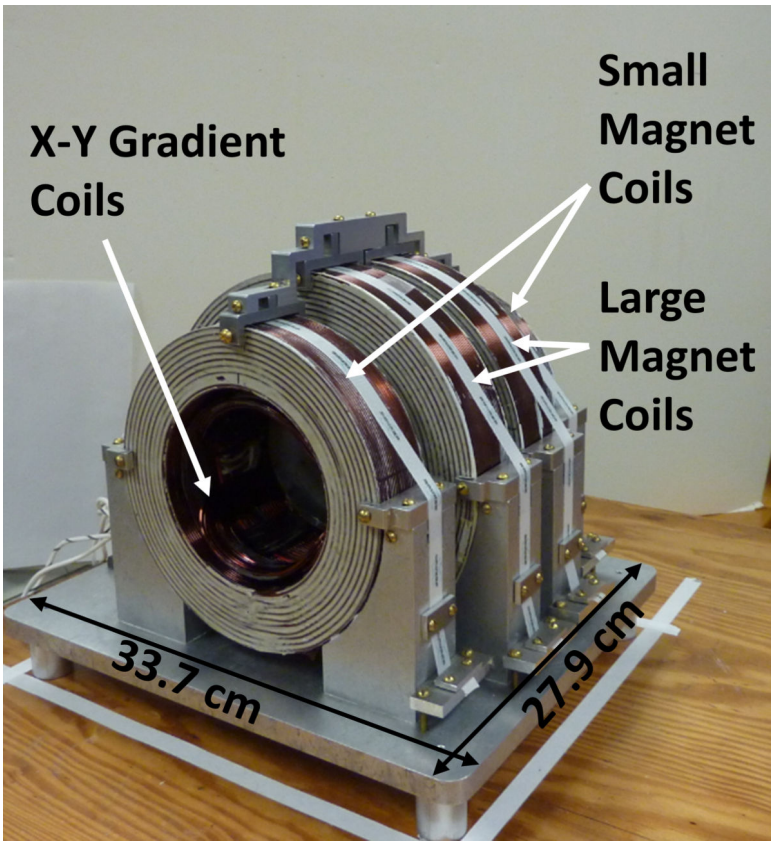

Figure 8.

Picture of 700 MHz magnet. The outer diameters of the small and large magnet coils are 18.2 and 22.6 cm, respectively. The inner diameter of the small coils is 11.3 cm. The Z-gradient coils are concentric with the main magnet coils, and fit inside the large magnet coils. The Z-gradient coils have the same inner diameter as the small magnet coils. The X-Y gradient saddle coils are pictured inside the main magnet and Z-gradient coils, and are shown in more detail in Figure 9.

Author Manuscript Author Manuscript Author Manuscript Author Manuscript

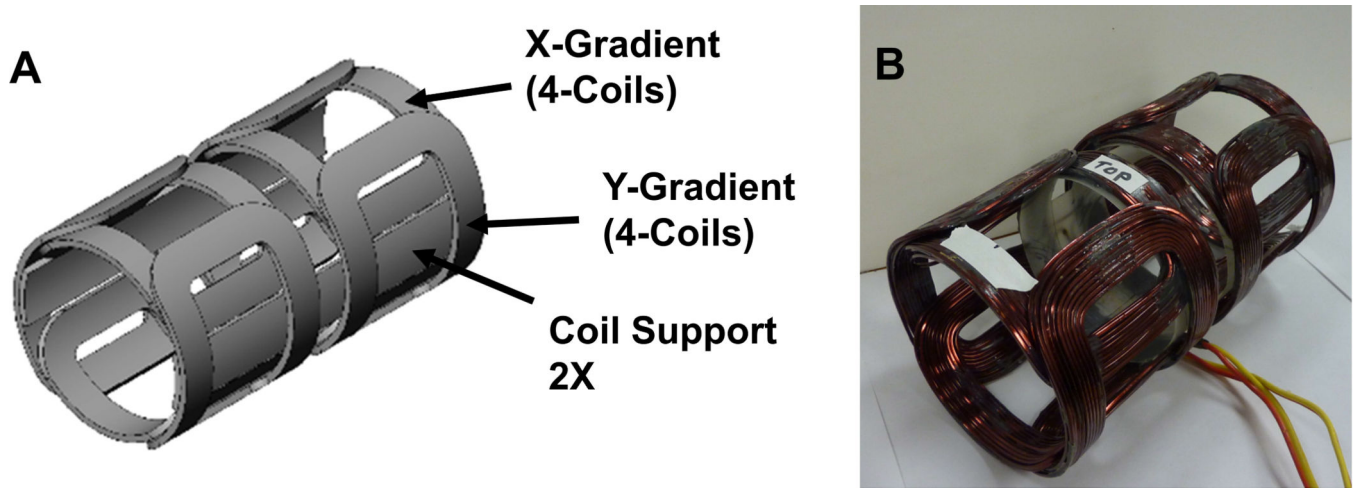

Figure 9.
(A) Drawing of X-, Y- gradient coils. (B) Picture of X-, Y- gradient coils.

Author Manuscript Author Manuscript Author Manuscript Author Manuscript

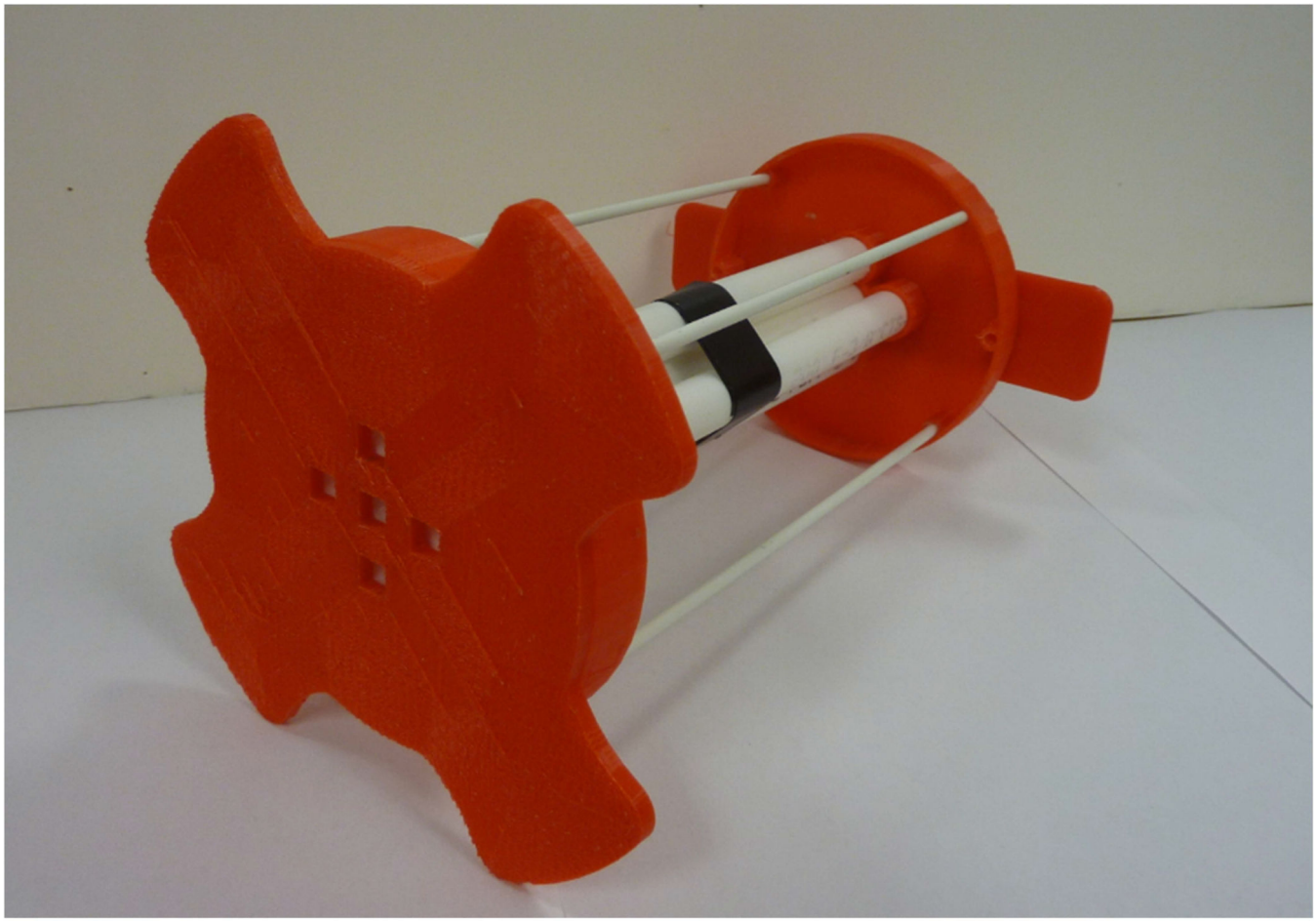

Figure 10.

3-D printed support structure for measuring the magnetic field uniformity. The structure fits inside the magnet system. The five slots shown in the front serve as a positioning system for the resonator shown in Figure 7A.

Author Manuscript Author Manuscript Author Manuscript Author Manuscript

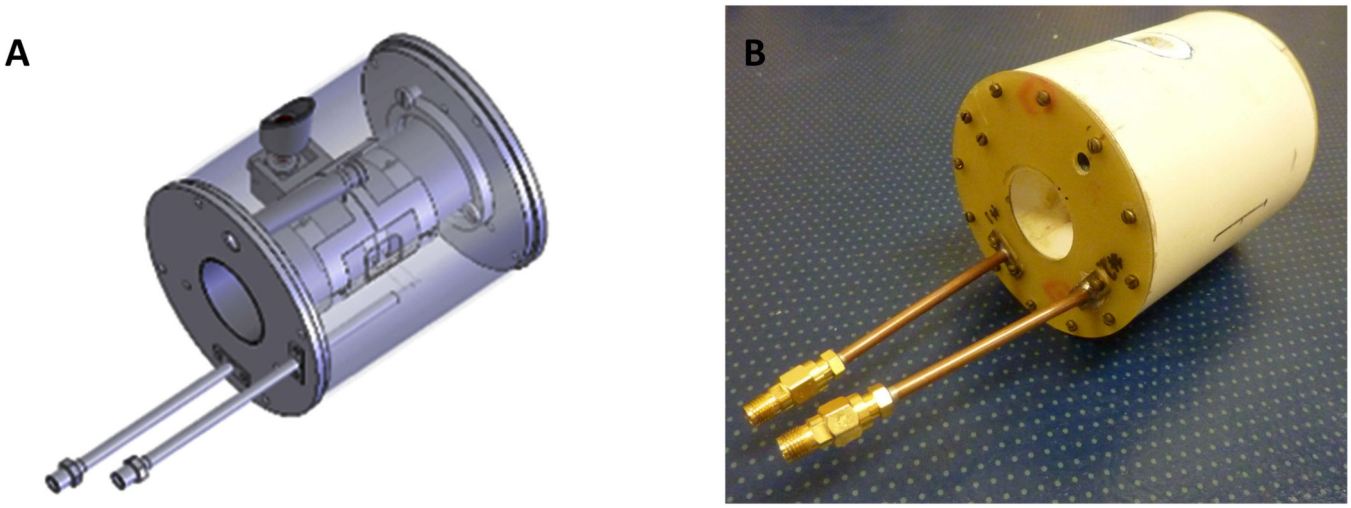

Figure 11.
(A) Drawing of 700 MHz cross-loop resonator. (B) Picture of 700 MHz cross-loop resonator.

Author Manuscript Author Manuscript Author Manuscript Author Manuscript

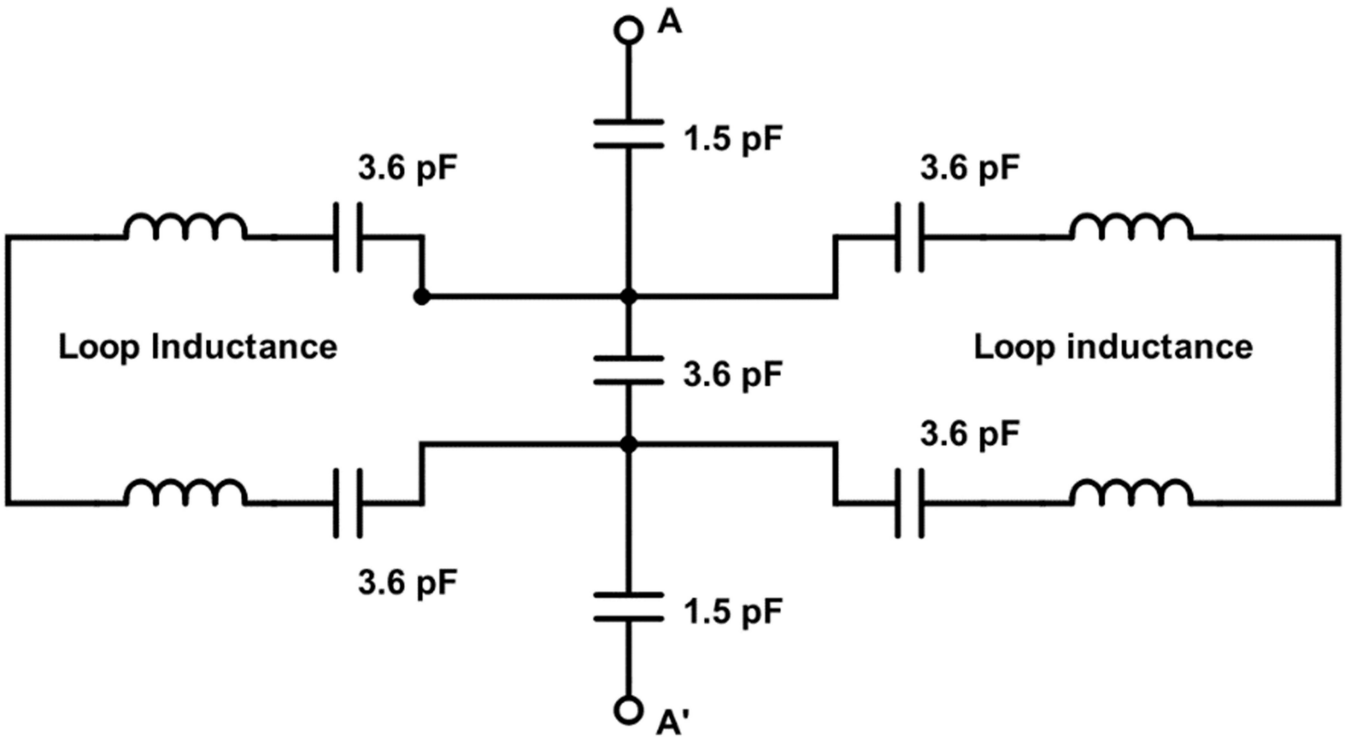

Figure 12.
Equivalent circuit for sample resonator.

Author Manuscript Author Manuscript Author Manuscript Author Manuscript

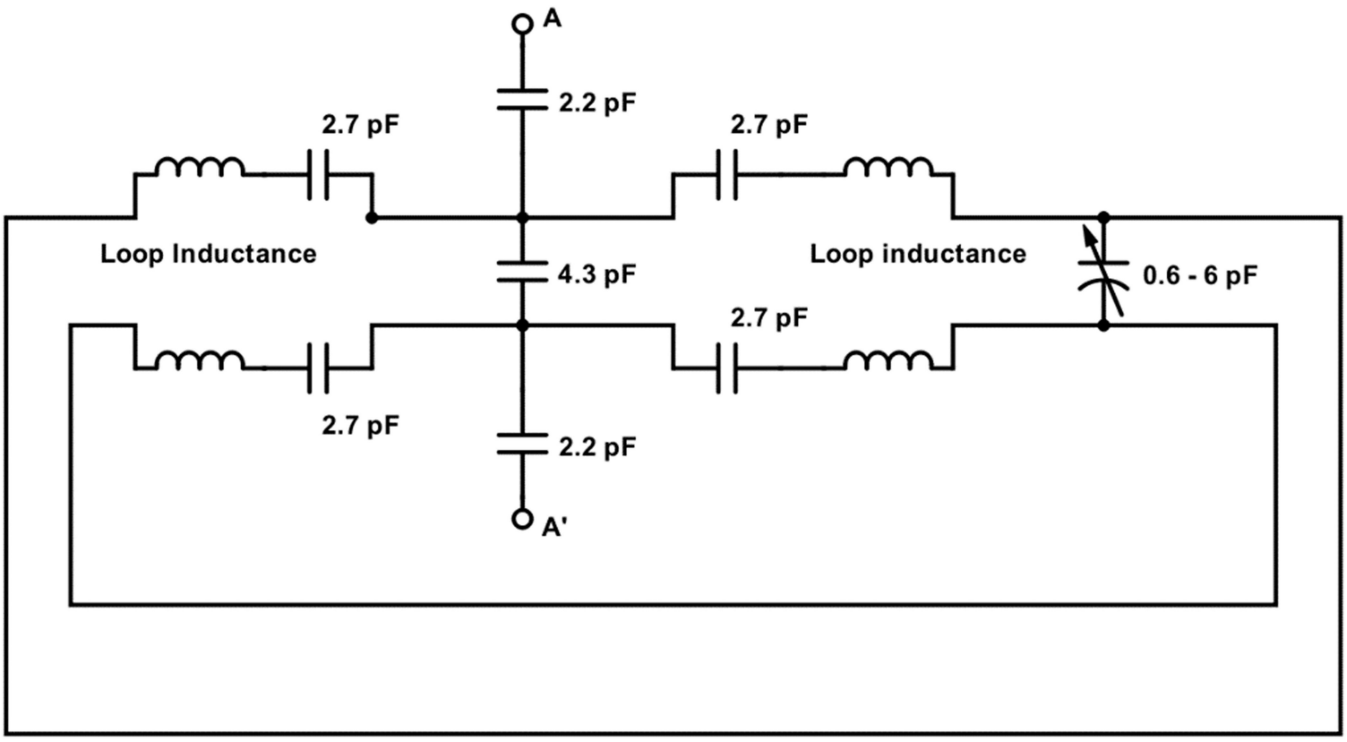

Figure 13.
Equivalent circuit for driven resonator.

Author Manuscript Author Manuscript Author Manuscript Author Manuscript

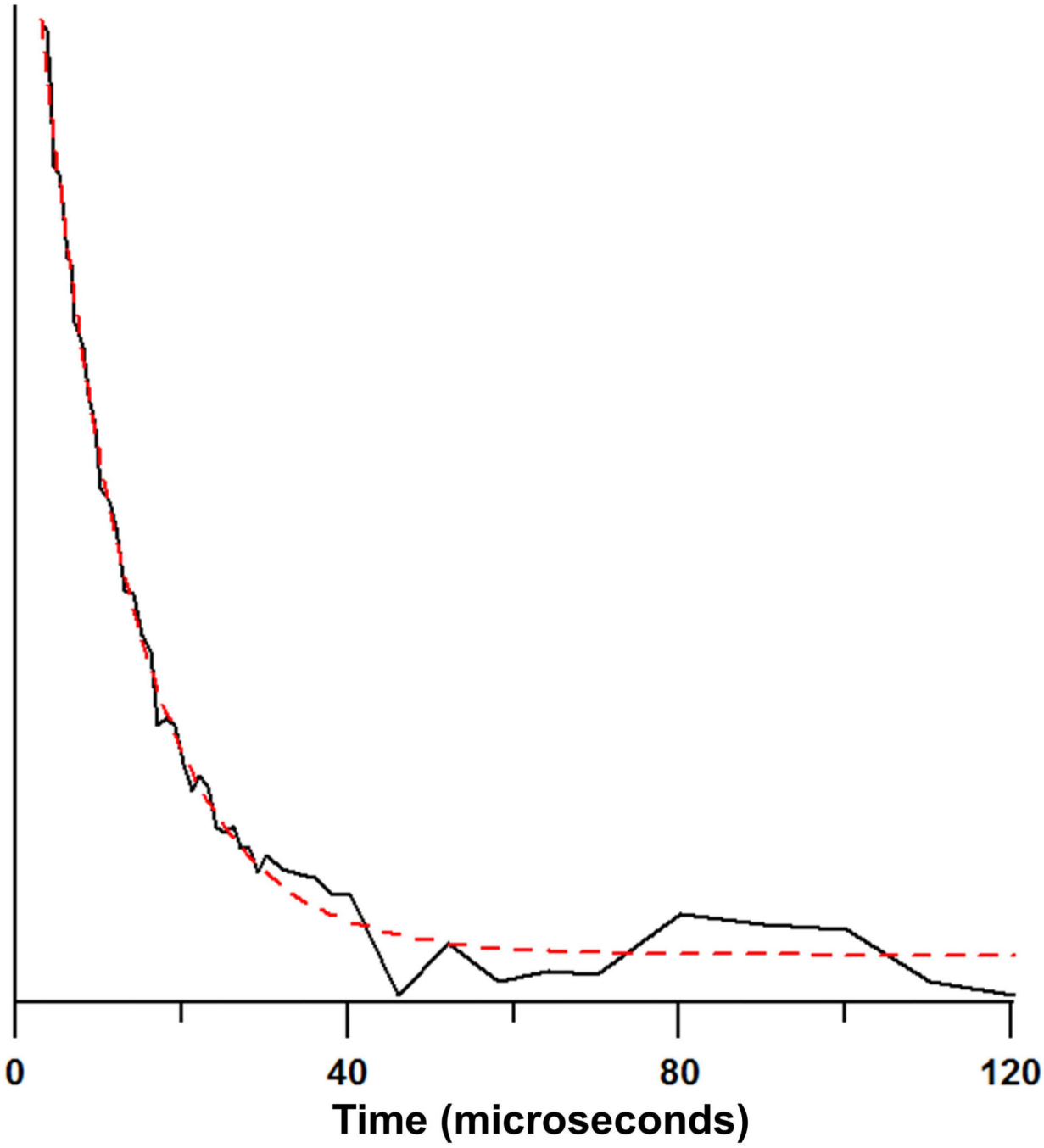

Figure 14.

Echo decay curve for 0.5 mM trityl-CD_3 (volume = 12.3 mL) in water. Dashed line is fit for T_m = 11.1 μs.

Author Manuscript Author Manuscript Author Manuscript Author Manuscript

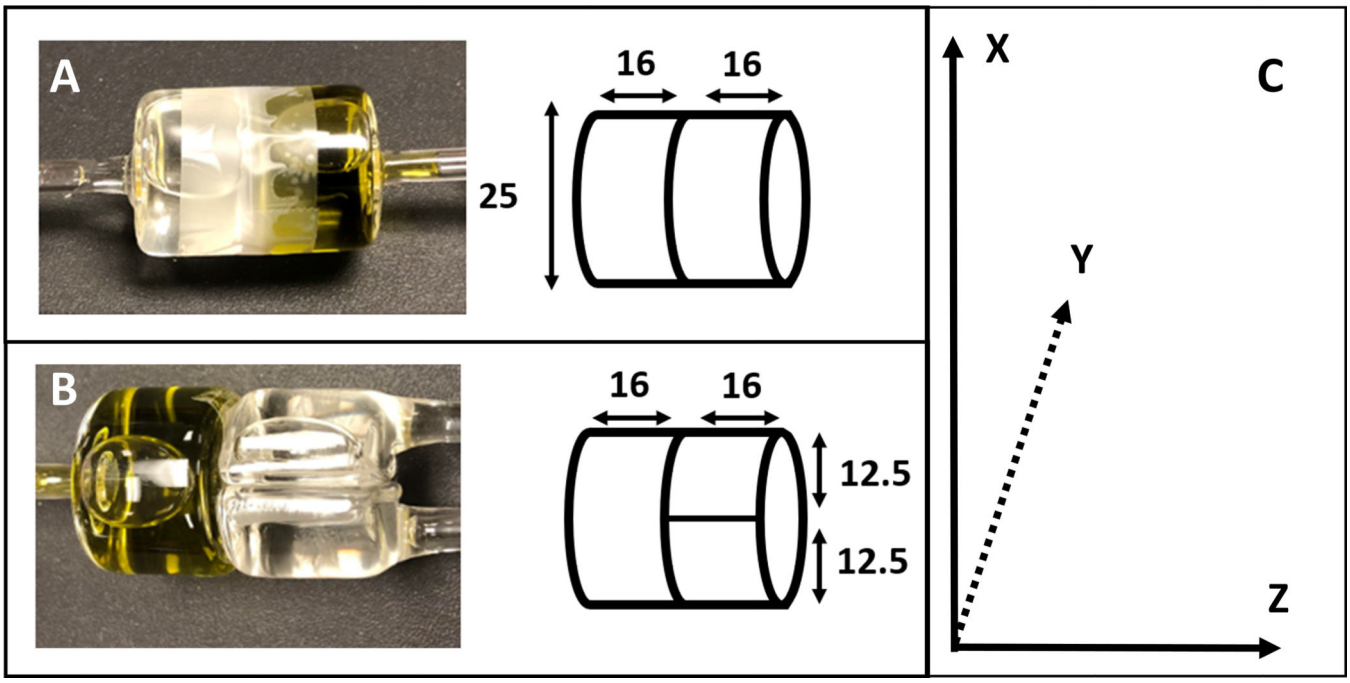

Figure 15.

Phantoms used for imaging. Dimensions are in mm. The wall thickness is about 1.5 mm for each tube. (A) The phantom for 4-D imaging consists of 1 mM ^{14}N Tempol (left), and 0.1 mM OX63 (right) separated along the Z axis. (B) The phantom used for 2-D imaging consists of 1 mM ^{15}N PDT (bottom right), 1 mM ^{14}N Tempol (top right), and 0.1 mM OX63 (left). The nitroxides are separated from each other along the X direction. The nitroxide is separated from OX63 along the Z axis. (C) Coordinate system for phantoms. The Y axis points into the page. Numerical values of positions shown in images are relative to 0,0,0 for the center of the reconstructed image.

Author Manuscript Author Manuscript Author Manuscript Author Manuscript

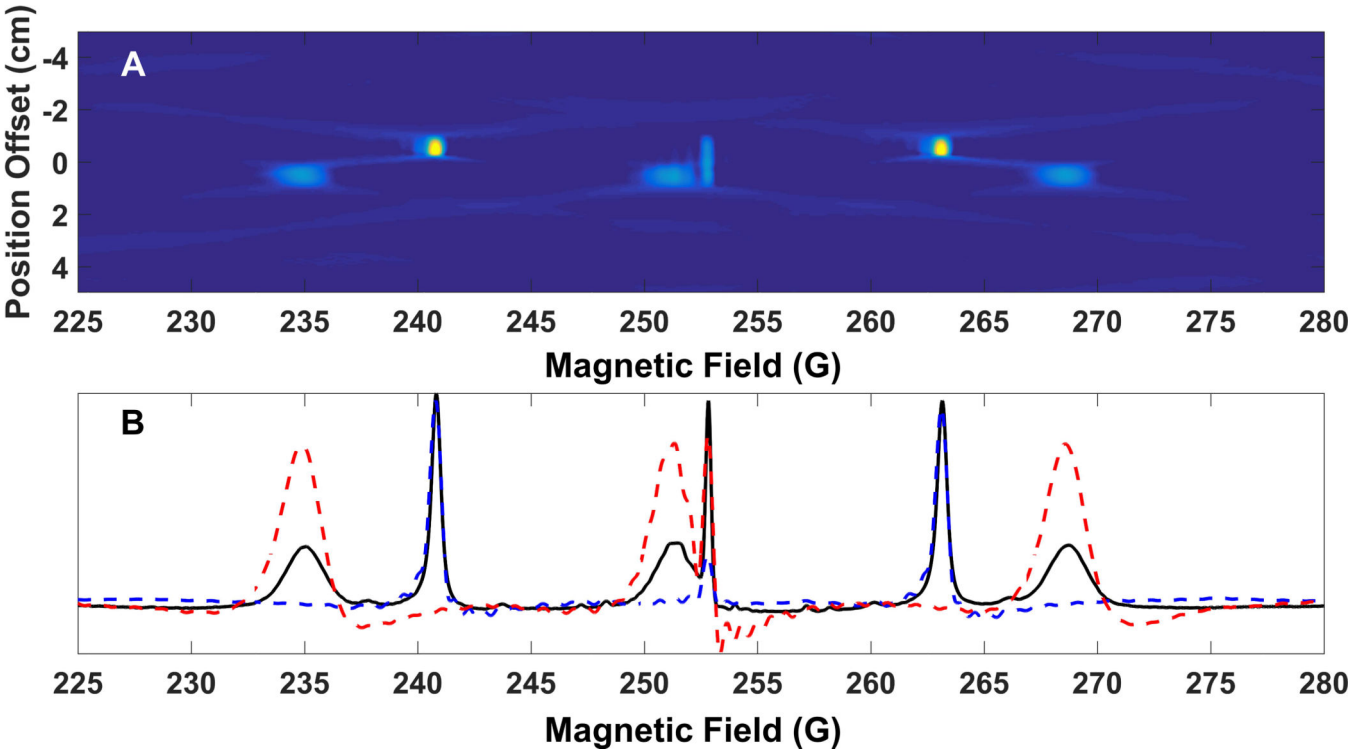

Figure 16.

2-D spectral-spatial image of phantom with three compartment that is shown in Figure 15B, obtained with gradient varied along the X axis. Top: reconstructed image. Bottom: Spectral slices along X = −0.53 cm (blue, dashed) and X = +0.48 cm (red, dashed). The solid black line is the nongradient spectrum. The OX63 signal is in both slices. The gradient along the X direction distinguishes between the ^{14}N Tempol in the lower compartment and the ^{15}N PDT in the upper compartment.

Author Manuscript Author Manuscript Author Manuscript Author Manuscript

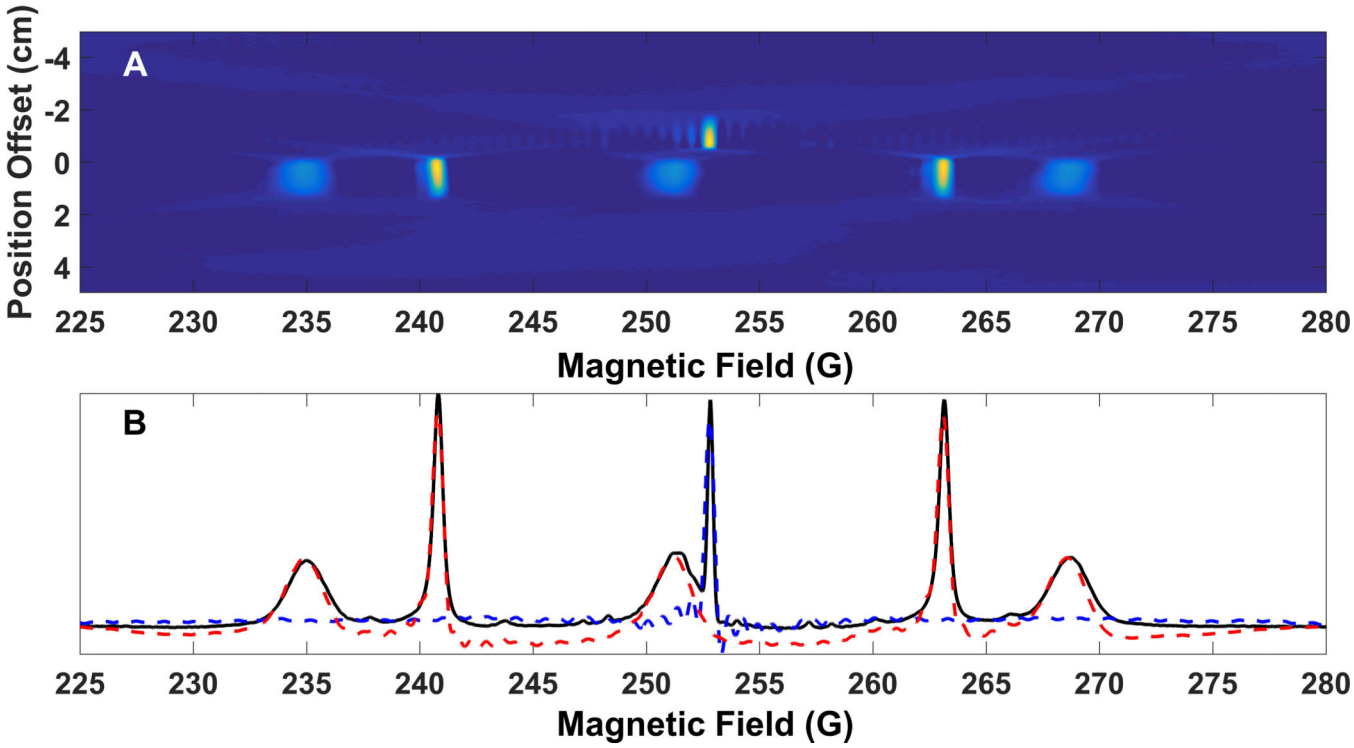

Figure 17.

2-D spectral-spatial image of three compartment phantom shown in Figure 15B with gradient was varied along the Z axis. Top: reconstructed image. Bottom: Spectral slices along Z = −0.85 cm (blue, dashed) and Z = +0.59 cm (red, dashed). The solid black line is the nongradient spectrum. The gradient along the Z axis distinguishes between the OX63 signal for Z < 0, but does not distinguish between the nitroxides in the two compartments with Z >0.

Author Manuscript Author Manuscript Author Manuscript Author Manuscript

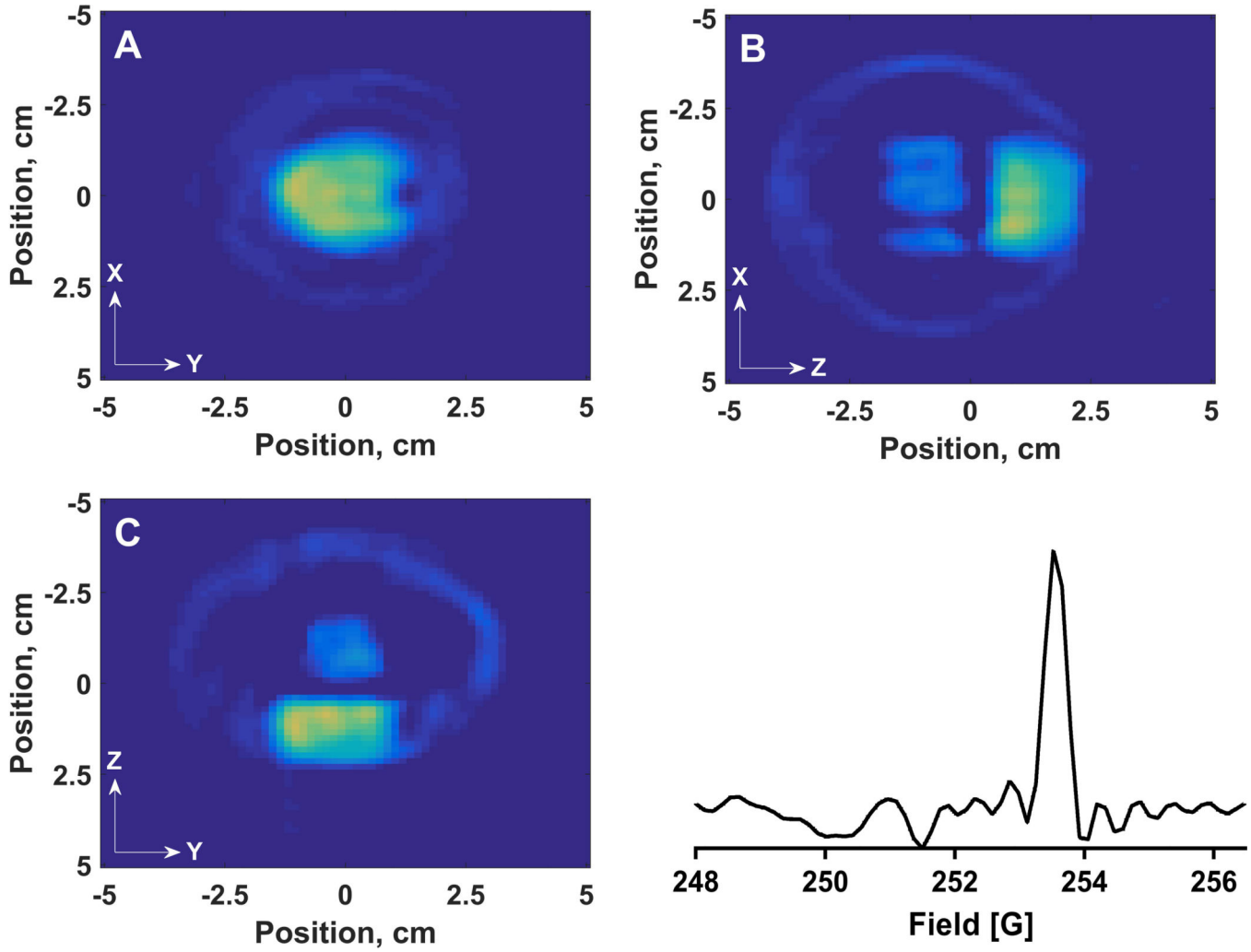

Figure 18.

Parts A-C show 2-D spatial slices through a 4-D image of the phantom in Figure 15A for the spectral region that includes the OX63 and central nitroxide line. (A) shows the intensity in an X-Y slice for fixed Z that is summed for Z = +0.87, +1.03, and +1.19 cm, which is the OX63 compartment. (B) shows the OX63 intensity in an X-Z slice for fixed Y = −0.08 cm. (C) shows the OX63 intensity in a Y-Z slice for fixed X = −0.08 cm. At each position in the 2-D spatial slices the intensity corresponds to the intensity at the magnetic field where the amplitude of the OX63 signal is maximum. The OX63 signal is superimposed on the high field wing of the broader nitroxide signal so some intensity is observed for the nitroxide compartments in B and C. (D) shows a spectral slice at X and Y = −0.08 cm and the sum of Z = = +0.87, +1.03, and +1.19 cm.

Author Manuscript Author Manuscript Author Manuscript Author Manuscript

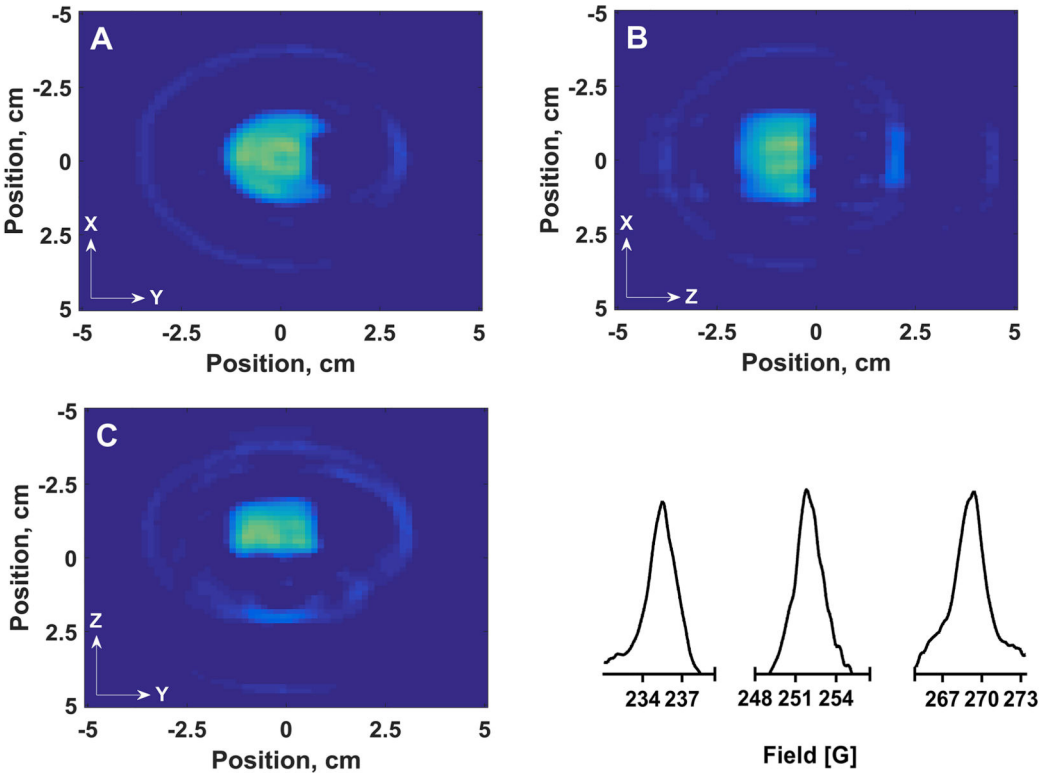

Figure 19.

Parts A-C show 2-D spatial slices through 4-D image of the phantom shown in Figure 15A. (A) shows the intensity in an X-Y slice for fixed Z that is summed for −0.87, −0.71, and −0.56 cm, which is the nitroxide compartment. (B) shows the nitroxide intensity in an X-Z slice for fixed Y = −0.08 cm. (C) shows the nitroxide intensity in a Y-Z slice for fixed X = −0.08 cm. At each position in the 2-D spatial slices the intensity is the sum of the nitroxide signals at the 3 magnetic fields where the amplitude is maximum. (D) shows three segments of the spectral slices, corresponding to the three lines of the nitroxide spectrum, calculated by summing the spectra at X and Y = −0.08 cm and the sum of Z = −0.87, −0.71, and −0.56 cm.

Author Manuscript

Author Manuscript

Author Manuscript

Table 1

List of components corresponding to the block diagram in Figure 2.

Reference Designator	Device Type	Manufacturer	P/N	Gain	Output Level
(A1)	Amplifier	MiniCircuits	ZRL-1200+	+30 dB	+29 dBm
(SW1)	Electronic Switch	MiniCircuits	ZFSWA2–63DR		
(SA1)	Step Attenuator	JFW	50DR-001SMA		
(SW2)	Electronic Switch	MiniCircuits	ZFSWA2–63DR		
(AT1)	Fixed Attenuator			−4 dB	
(A2)	Amplifier	MiniCircuits	ZHL-1010+	+10 dB	+30 dBm
(PH1)	Voltage controlled phase shifter	Bel Power Solutions	HP1001		360° for 10 V input
(A3)	Amplifier	MiniCircuits	ZX60–2522M-S+	+21 dB	+18 dBm
(SW3)	Electronic Switch	MiniCircuits	ZX80-DR230-S+		
(SW4)	Electronic Switch	MiniCircuits	ZX80-DR230-S+		
(SW5)	Mechanical Switch	MiniCircuits	MSPT-2–18-12+		
(SW6)	Electronic Switch	MiniCircuits	ZX80-DR230-S+		
(DC1)	Directional Coupler	MiniCircuits	ZFDC-15–5-S+	−15 dB	
(B1)	Electronic Switch	MiniCircuits	ZASWA-2–50DR+		
(HPF1)	High Pass Filter	MiniCircuits	SHP-700+		
(SW7)	Mechanical Switch	MiniCircuits	MSPT-2–18-12+		
(LIM1)	Limiter	MiniCircuits	VLM-33-S+		
(A4)	Amplifier	MiniCircuits	ZX60-P33ULN+	+20 dB	+17.5 dBm
(TS1)	Transfer Switch	MiniCircuits	MTS-18–12B		
(DC2)	Directional Coupler	MiniCircuits	ZX30–20-4	−20 dB	
(C1)	Circulator	UTE Microwave Inc	CT-1260-O		

Author Manuscript

Author Manuscript

Author Manuscript

Author Manuscript

Table 2.

Switching logic for tune and operate paths.[a]

Path	SW1	SW2	SW3	SW4	SW5	SW6	SW7	TS1
Tune CLR 1	C-1	C-1	C-2	C-1	C-NO	–	C-NO	1–2/3–4
Tune CLR 2	C-1	C-1	C-2	C-2	–	C-2	C-NO	1–2/3–4
Isolation/ Tune LGR	C-1	C-1	C-1	–	C-NC	C-1	C-NC	1–2/3–4
Operation	C-1	C-1	C-1	–	C-NC	C-1	C-NC	1–3/2–4

[a]The labeling of the switches is shown in Figure 2. An entry such as C-1 means that common position of the electronic switch is connected to output 1. An entry such as C-NO means that a mechanical switch is in the position that is identified as normally open.

Author Manuscript

Author Manuscript

Author Manuscript

Author Manuscript

Table 3

Noise figure and gain values used for Friis equation.

	Noise Figure (dB)	Gain (dB)
Loss Before First Stage	+6.7	−6.7
First Stage Amplifier (A4)	+0.4	+20.98
Loss Between First and Second Stage Amplifiers	+5.5	−5.5
Second Stage Amplifier	+15.4	+40

Author Manuscript

Author Manuscript

Author Manuscript

Author Manuscript

Table 4

Residual nonuniformity in magnetic field over the sample space before and after corrections with gradient coils measured. Ppm is calculated out of 252 G.

Axis	Residual gradients - No corrections (G/cm)	Residual gradients - With corrections (G/cm)
X	0.034 (135 ppm)	0.001 (4 ppm)
Y	0.049 (194 ppm)	0.002 (8 ppm)
Z	0.006 (24 ppm)	0.006 (24 ppm)

Author Manuscript

Author Manuscript

Author Manuscript

Author Manuscript

Table 5

Gradient coil characteristics

Gradient Coil	Coil Constant	Inductance (mH)	Resistance (Ω)
X	0.74 G/A – 0.03 G	0.24	0.28
Y	0.8 G/A – 0.04 G	0.24	0.28
Z	1.88 G/A	1.6	0.28